bioRxiv preprint doi: https://doi.org/10.1101/2022.06.29.498001; this version posted July 2, 2022. The copyright holder for this preprint (which was not certified by peer review) is the author/funder. All rights reserved. No reuse allowed without permission.

Biofunctional matrix models reveal mineral-dependent mechanoregulation of bone metastatic breast cancer

Siyoung Choi[1, +], Matthew A. Whitman[1, +], Adrian A. Shimpi[1], Aaron Chiou[1], Joseph E. Druso[1], Akanksha Verma[3], Stephanie C. Lux[1], Zhu Cheng[2], Matthew Paszek[2], Olivier Elemento[3], Lara A. Estroff[4, 5*] and Claudia Fischbach[1, 5*]

[1] Nancy E. and Peter C. Meinig School of Biomedical Engineering, Cornell University, USA.

[2] Robert Frederick Smith School of Chemical and Biomolecular Engineering, Cornell University, USA

[3] Caryl and Israel Englander Institute for Precision Medicine, Institute for Computational Biomedicine, Weill Cornell Medicine, USA.

[4] Department of Materials Science and Engineering, Cornell University, USA.

[5] Kavli Institute at Cornell for Nanoscale Science, Cornell University, USA

[+]These authors contributed equally.

*To whom correspondence should be addressed:

cf99@cornell.edu

lae37@cornell.edu

bioRxiv preprint doi: https://doi.org/10.1101/2022.06.29.498001; this version posted July 2, 2022. The copyright holder for this preprint (which was not certified by peer review) is the author/funder. All rights reserved. No reuse allowed without permission.

Abstract

Bone metastasis is a leading cause of death among patients with advanced breast cancer, but the mechanisms controlling tumor cell phenotype in the skeleton remain elusive. In particular, it is unknown how bone matrix mineralization dictates cellular entry to latency or metastatic outgrowth. Understanding these connections is critical given that tumor cells often disseminate to regions of active mineralization. Using biofunctional models of bone matrix, we show that matrix mineralization is a critical and largely overlooked component determining the early-stage development of bone metastases. Contradicting the conventional assumption that rigidity stimulates metastatic progression, we found that tumor cell proliferation changes with matrix mineralization where higher mineral levels, which increased rigidity, induced quiescence by reducing mechanosignaling. This matrix-inducible phenotype is durable to changes in mineral content and translated to reduced tumor growth *in vivo* and patient mortality. Our results suggest that methods to maintain physiological bone matrix mineralization could be leveraged clinically to promote quiescence in patients with advanced disease and that models for studies of bone metastasis should integrate mineral as a key design parameter.

bioRxiv preprint doi: https://doi.org/10.1101/2022.06.29.498001; this version posted July 2, 2022. The copyright holder for this preprint (which was not certified by peer review) is the author/funder. All rights reserved. No reuse allowed without permission.

Introduction

Breast cancer frequently metastasizes to bone where it leads to osteolysis and poor clinical prognosis[1–3], but therapies to treat or prevent bone metastasis are lacking. Most prior research has focused on clinically apparent bone degradation uncovering that unbalanced osteoclast activity and consequential activation of the 'vicious cycle of bone metastasis' allows asymptomatic, residual disease to develop into overt metastasis[4,5]. However, how tumor cells initially colonize and survive in the skeletal microenvironment is poorly understood. Indeed, tumor cells can disseminate to bone very early during tumor development and enter a state of latency in which they proliferate less and assume stem cell-like properties[6–8]. Activation of these latent tumor cells to a more proliferative phenotype contributes to their outgrowth into metastatic tumors after years or even decades[7]. As microenvironmental conditions are key determinants of tumor cell latency and stemness[8], it will be critical to better define how bone-specific niches and changes thereof influence the stem-like phenotype of tumor cells in the skeleton.

While most research on early-stage bone metastasis focuses on the marrow, tumor cells also colonize osteogenic niches in the skeleton. These niches consist of osteoblasts and their progenitors whose hallmark function is to deposit and mineralize extracellular matrix (ECM)[9,10] (Fig. 1a). Conditions affecting osteoblasts and their progenitors (e.g., aging or chemotherapy) inhibit the formation of mineralized matrix and alter the secretome of osteoblast-lineage cells[11,12]. While the latter has been shown to regulate metastatic latency[13] and outgrowth[11,12], it remains underappreciated how varied bone ECM formation and mineralization influence tumor cell phenotype. Better understanding these connections will be important as changes of the ECM play a key role in regulating tumor cell phenotype and because disseminated cancer cells directly interact with the matrix[9,14].

bioRxiv preprint doi: https://doi.org/10.1101/2022.06.29.498001; this version posted July 2, 2022. The copyright holder for this preprint (which was not certified by peer review) is the author/funder. All rights reserved. No reuse allowed without permission.

During osteogenesis, osteoblasts first deposit osteoid, the collagen I-rich, unmineralized component of bone ECM, within which carbonated hydroxyapatite (HA; $Ca_{10}(PO_4,CO_3)_6(OH)_2$) nanoparticles subsequently form[15,16] (Fig. 1a). This process of mineralization is accompanied by distinct changes in bone matrix mechanical properties (e.g., increased stiffness, reduced stress relaxation[17]), which can impact tumor cell phenotype through altered mechanosignaling[18,19]. Moreover, bone matrix mineralization is a dynamic process that changes as a function of anatomical site, age, and disease[20–23]. How changes in bone matrix mineralization influence the phenotype of tumor cells, however, remains unclear due in part to a lack of model systems that allow control over bone matrix mineral content for mechanistic studies. Studies with such systems will be critical to elucidate why reduced bone formation and local mineral density increase the risk for bone metastasis[12,24], whereas conditions promoting new bone formation and mineralization inhibit bone metastasis[25,26].

Conventional models of breast cancer (i.e., 2-D cell culture and mouse models) fail to recapitulate *(i)* compositional, structural, and mechanical alterations of bone matrix and *(ii)* do not allow control over the level of mineralization that changes during osteogenesis and as a function of age and disease[22,23,27]. Moreover, conventional mineralization methods deposit HA on top of collagen rather than integrate it within fibers as occurs in physiological mineralization, with consequences on substrate mechanical properties. Here, we have developed osteoid-like and bone-like scaffolds in which we can selectively adjust bone matrix mineral content for both *in vitro* and *in vivo* experiments. These model systems include: *(i)* 2.5-D collagen matrices in which we synthetically control bone-like intrafibrillar mineralization through a modified polymer-induced liquid precursor (PILP) method[28] and *(ii)* decellularized trabecular bone scaffolds in which we can selectively remove mineral without affecting organic ECM composition and microstructure. Using

bioRxiv preprint doi: https://doi.org/10.1101/2022.06.29.498001; this version posted July 2, 2022. The copyright holder for this preprint (which was not certified by peer review) is the author/funder. All rights reserved. No reuse allowed without permission.

these biofunctional scaffolds, we probed the role of bone matrix mineralization in regulating the phenotype of breast cancer cells *in vitro* and tested which role mechanosignaling plays in this process. Then, we evaluated the impact of our results on tumor growth in mice and on patient prognosis using computational analysis of METABRIC and TCGA data sets. Collectively, our results suggest that the mineral content of bone matrix regulates skeletal metastasis by influencing the phenotype of breast cancer cells. These findings could lead to the development of improved therapies and highlight the importance of relevant model systems for studies of breast cancer bone metastasis.

Results

Disseminated tumor cells seed mineralizing bone niches, which can be mimicked by intrafibrillar mineralization of collagen.

Whether disseminated tumor cells localize to skeletal regions of new matrix mineralization is poorly characterized given the intrinsic difficulty of imaging rare numbers of tumor cells within fully intact, highly autofluorescent, mineralized bones. To circumvent this challenge, we have labeled MDA-MB231 breast cancer cells with bright fluorescent silica nanoparticles and intracardially injected them into athymic nude mice in which newly mineralizing bone surfaces were labeled with calcein[29]. As expected, cancer cells localized to niches within the marrow in this model[30]. However, light sheet microscopy of cleared mouse tibiae also revealed that tumor cells co-localized with regions of new matrix mineralization (Fig. 1b) consistent with previous results identifying the osteogenic niche as a target for early-stage bone colonization[9].

To investigate whether bone matrix mineralization alone affects the phenotype of tumor cells, we utilized a bone-like ECM platform in which we induced biofunctional intrafibrillar mineralization of collagen using a modified polymer-induced liquid-precursor (PILP) method[28,31]. Briefly,

bioRxiv preprint doi: https://doi.org/10.1101/2022.06.29.498001; this version posted July 2, 2022. The copyright holder for this preprint (which was not certified by peer review) is the author/funder. All rights reserved. No reuse allowed without permission.

collagen was cast into polydimethylsiloxane (PDMS) microwells or on glass coverslips and mineralized in a solution containing calcium and phosphate ions as well as polyaspartic acid to control the formation of HA nanocrystals within collagen fibrils (Fig. 1c). In this system, the polyaspartic acid serves a function similar to non-collagenous proteins in bone, resulting in the formation of bone-like mineralized collagen fibers[18]. Scanning electron microscopy (SEM) image analysis confirmed that mineralization did not impact the fibrous architecture of collagen but increased the thickness of individual fibrils (Fig. 1d, e) due to mineral formation as confirmed by backscattered electron (BSE) imaging (Fig. 1d). Fourier transform infrared (FT-IR) and powder X-ray diffraction (pXRD) further identified that the chemical composition and phase of the newly formed mineral were consistent with HA (Fig. 1f, g). FT-IR spectra of both control and mineralized collagen contained characteristic protein amide peaks between 1200 - 1700 cm^{-1}, while PO_4^{3-} peaks indicative of HA (500-700 cm^{-1} and 900-1200 cm^{-1}) were only detected in mineralized collagen (Fig. 1f). Moreover, the mineral content of these matrices was comparable to human bone as suggested by FT-IR analysis of the mineral to matrix ratio (Supplementary Fig. 1; mineralized collagen: approx. 4; human bone: 3-6)[20]. Finally, the phase of the mineral that formed in collagen was similar to the poorly crystalline, non-stoichiometric carbonated apatite in bone[32] as indicated by the presence and broadening of pXRD peaks at 26° and 32° (Fig 1g). Taken together, these results indicate that bone-like collagen-HA composites can be formed by synthetic intrafibrillar collagen mineralization.

Collagen mineralization alters breast cancer cell gene expression and growth *in vitro*.

As microfabricated collagen and mineralized collagen substrates recapitulated the two extremes of bone matrix mineralization (i.e., non-mineralized osteoid vs. fully mineralized bone matrix), we

bioRxiv preprint doi: https://doi.org/10.1101/2022.06.29.498001; this version posted July 2, 2022. The copyright holder for this preprint (which was not certified by peer review) is the author/funder. All rights reserved. No reuse allowed without permission.

next used these substrates to test how bone matrix mineralization affects tumor cell phenotype. When cultured on mineralized versus control collagen metastatic MDA-MB231 breast cancer cells spread less and exhibited reduced remodeling of their surrounding collagen network as indicated by limited fiber alignment and densification that is known to mediate local strain stiffening in control collagen[33] (Fig. 2a, b). Consistent with these morphological differences principal component analysis (PCA) of bulk RNA-seq data sets suggested that collagen mineralization globally affects gene expression of MDA-MB231 (Fig. 2c). Differential gene expression analysis further identified that genes associated with breast cancer metastasis (ANGPTL2, CAMK1D, CEMIP)[34–36] and stemness (B4GALNT3, TRIB3)[37,38] were among the top 50 differentially expressed genes in the mineralized collagen condition, while most of the top 50 ranked genes regulated by collagen were linked with cell cycle (CDCA7, CHTF18, DBF4B, KIF18B) (Fig. 2d, Table 1, Supplementary Fig. 2). Gene set enrichment analysis (GSEA) confirmed that cell cycle-related gene sets, most prominently DNA replication, were over-represented in cells cultured on collagen, while gene sets associated with stress response and ECM disassembly were over-represented in cells cultured on mineralized collagen (Fig. 2e). These results suggest that bone matrix mineralization impacts breast cancer cell functions centrally implicated in bone metastasis.

As gene sets related to cell-cycle related pathways were most prominently affected by changes in collagen mineralization, we next measured tumor cell growth on the different substrates. Both MDA-MB231 bromodeoxyuridine (BrdU) incorporation and DNA content was reduced by culture on mineralized collagen relative to collagen, indicating decreased proliferation under these conditions (Fig. 2f, g). Accordingly, collagen mineralization also reduced growth of the bone tropic MDA-MB231 subclone BoM1-2287[18] and estrogen-receptor positive MCF-7 cells supporting that our findings were not limited to MDA-MB231 (Fig. 2g). Next, we evaluated if this

bioRxiv preprint doi: https://doi.org/10.1101/2022.06.29.498001; this version posted July 2, 2022. The copyright holder for this preprint (which was not certified by peer review) is the author/funder. All rights reserved. No reuse allowed without permission.

decreased proliferative state is reversible in scenarios that lead to decreased matrix mineralization (e.g. aging, chemotherapy, osteolysis)[22,23,39]. To this end, we precultured MDA-MB231 on collagen and mineralized collagen for 7 days, a timeframe reported to cause irreversible phenotypic changes[40,41], and then reseeded them onto either collagen or mineralized collagen (Fig. 2h). Indeed, cells pre-cultured on mineralized collagen assumed a more proliferative phenotype when reseeded onto non-mineralized collagen albeit at reduced levels relative to cells that were precultured on collagen. In contrast, reseeding of cells onto mineralized collagen significantly decreased tumor cell growth irrespective of the substrate on which cells were cultured previously (Fig. 2h). These data indicate that collagen mineralization reduces tumor cell growth in a reversible manner possibly contributing to metastatic outgrowth under conditions of reduced matrix mineralization during later stages of the disease.

Mineralized collagen increases a stem-like phenotype in breast cancer cells.

Motivated by our observation that collagen mineralization reduces tumor cell proliferation (Fig. 2), a hallmark of quiescent stem-like tumor cells[8,42], and because dissemination to bone confers stem-like properties on cancer cells[43], we next determined whether mineralized collagen regulates the stem-like phenotype of breast cancer cells. These experiments were performed with an MDA-MB231 stem cell reporter cell line that expresses GFP as a function of Nanog promoter activity[44], which we validated to correlate with expression of two other stem cell markers, Oct4 and Sox2 (Fig. 3a). Flow cytometry and confocal image analysis indicated that culture on mineralized collagen increased the number of GFP^{high} cells relative to culture on collagen or polystyrene (Fig. 3a, b). To confirm these changes were driven by mineral, we performed a dose response study in which substrates of controlled HA content were fabricated by dissolving HA from fully

bioRxiv preprint doi: https://doi.org/10.1101/2022.06.29.498001; this version posted July 2, 2022. The copyright holder for this preprint (which was not certified by peer review) is the author/funder. All rights reserved. No reuse allowed without permission.

mineralized collagen at physiological pH for up to 6 days, a process that selectively removed HA without affecting collagen microstructure (Fig. 3c, Supplementary Fig. 3). Decreasing mineral content reduced the percentage of Nanog-GFP positive cells supporting that collagen mineralization directly regulates the stem-like phenotype of breast cancer cells (Fig. 3d). Further validating the induction of stemness by mineral, parental MDA-MB231 cultured on mineralized collagen also exhibited increased activity of the stem cell marker aldehyde dehydrogenase (ALDH)[45,46] (Fig. 3e). Moreover, MDA-MB231 precultured on mineralized collagen formed more colonies in soft agar relative to the same cells precultured on polystyrene or collagen indicating that interactions with mineralized collagen endow tumor cells with survival advantages in adhesion-independent scenarios (Fig. 3f).

Mineralized collagen regulates breast cancer cell phenotype by altering mechanosignaling. Increased cell adhesion forces are drivers of tumor cell growth and typically increased on stiffer matrices[47]. While mineralization increases collagen stiffness, it simultaneously reduces collagen stress relaxation resulting in decreased rather than increased cell adhesion forces with consequential changes in cell spreading and collagen network remodeling (Fig. 2a, b)[17,18,48]. Because of these connections, we hypothesized that mineral-induced changes of mechanosignaling may be responsible for the above-described changes in tumor cell phenotype. To define which role mineralization-dependent changes in mechanotransduction play in regulating tumor cell growth, we cultured MDA-MB231 on collagen and mineralized collagen in the presence and absence of β1-integrin blocking antibodies and pharmacological inhibitors of FAK (FAK inhibitor 14), ROCK (Y27632), and PI3K (LY294002) (Fig. 4a). Treatment with these reagents reduced tumor cell growth on collagen as expected but had no effect on mineralized collagen suggesting that

bioRxiv preprint doi: https://doi.org/10.1101/2022.06.29.498001; this version posted July 2, 2022. The copyright holder for this preprint (which was not certified by peer review) is the author/funder. All rights reserved. No reuse allowed without permission.

tumor cell mechanosignaling may be reduced on mineralized collagen. Tumor cells interacting with collagen have been described to increase their adhesion forces by aligning collagen fibers in a process that activates mechanosignaling via a positive feedback mechanism[33]. To test whether collagen mineralization interferes with this process by preventing cell-mediated collagen network remodeling as described above (Fig. 2b) and thus, reciprocal activation of cellular adhesion forces[18], we performed traction force microscopy. Indeed, consistent with the limited effect of mechanosignaling inhibitors on tumor growth, MDA-MB231 pre-cultured on mineralized collagen exhibited reduced cellular traction forces relative to their counterparts precultured on collagen or polystyrene (PS) (Fig. 4b, Supplementary Fig. 4) and sorted GFP^{high} cells exhibited similarly reduced traction forces relative to GFP^{low} cells (Fig. 4c). Collectively, these results suggest that collagen mineralization regulates the phenotype of breast cancer cells by inhibiting cell-mediated collagen remodeling that would otherwise increase growth by activating mechanosignaling.

Mineral content in native bone matrix regulates breast cancer cell phenotype similar to mineralized collagen.

In addition to collagen type I, the bone ECM contains other proteins (collectively referred to as noncollagenous proteins or NCPs) that may impact the response of tumor cells to mineral[49]. Additionally, the microfabricated collagen substrates described above are not suitable to validate *in vitro* results in a xenograft setting. To circumvent both limitations, we generated millimeter-sized physiological bone matrices in which we selectively controlled mineral content by adapting previously established protocols[50,51]. First, bone plugs were harvested from neonatal bovine femurs and fully decellularized to prepare scaffolds that contained all organic and inorganic matrix components including mineral but were devoid of cells (termed decellularized scaffolds [DC] from

bioRxiv preprint doi: https://doi.org/10.1101/2022.06.29.498001; this version posted July 2, 2022. The copyright holder for this preprint (which was not certified by peer review) is the author/funder. All rights reserved. No reuse allowed without permission.

here on). Next, DC scaffolds were demineralized with ethylenediaminetetraacetic acid (EDTA) resulting in decellularized and demineralized (DCDM) scaffolds (Fig. 5a). Adequate decellularization was verified histologically and by DNA assay[52] (Fig. 5b). Demineralization of DCDM was confirmed by nano-CT and FT-IR, while SEM, second harmonic generation (SHG) microscopy, and histological analysis confirmed that scaffold architecture and collagen fibrillar structure were not affected by the demineralization procedure (Fig. 5c, Supplementary Fig. 5a, b). Moreover, the pXRD patterns of DC scaffolds as well as their mineral to matrix ratio were comparable to physiological bone (and mineralized collagen) suggesting that the decellularization step had no effect on the mineral phase (Fig. 5d, e). Crystallinity of the HA in the DC scaffolds was also comparable to naïve bone but reduced relative to HA in mineralized collagen or pure HA, a difference that may be explained by the young age of the animals from which the bone was harvested (Fig. 5f).

After characterizing the bone scaffolds and confirming by SEM that MDA-MB231 cells adhered to and grew within the 3D scaffolds (Fig. 5g), we asked whether proliferation and stem-like behavior of breast cancer cells were altered by the different scaffold conditions. DNA analysis identified that cell growth within DC scaffolds was lower than that within DCDM scaffolds, supporting that the presence of mineral reduces breast cancer cell growth in these systems (Fig. 5g). Confocal imaging and flow cytometry of Nanog-GFP MDA-MB231 showed that breast cancer cells increased GFP expression and assumed more stem-like phenotypes when grown within mineral-containing DC scaffolds relative to PS and DCDM scaffolds (Fig. 5h). Taken together, these results indicate that the presence of mineral alters breast cancer cell behavior in physiological bone scaffolds similarly to the synthetic mineralized collagen scaffolds and thus, validate the broader significance of mineral to regulating tumor cell phenotypes.

bioRxiv preprint doi: https://doi.org/10.1101/2022.06.29.498001; this version posted July 2, 2022. The copyright holder for this preprint (which was not certified by peer review) is the author/funder. All rights reserved. No reuse allowed without permission.

Bone mineral affects breast cancer progression *in vivo*.

To test the relevance of bone matrix mineralization to tumor growth *in vivo*, decellularized physiological bone matrices with (DC) and without mineral (DCDM) (Fig. 5a) were seeded with luciferase-expressing MDA-MB231s, xenografted into female, athymic Nude-*Foxn1*^{nu} mice, and then tracked longitudinally by bioluminescence (BLI) imaging (Fig. 6a). Tumor cells interacted with trabecular surfaces of both scaffold types but grew significantly more on matrices devoid of mineral (Fig. 6b, c). Accordingly, co-immunostaining against human vimentin and Ki67 confirmed that tumors in mineral-containing DC scaffolds contained fewer human tumor cells than their DCDM counterparts and that tumor cells were less proliferative relative to tumor cells growing in DC scaffolds (Fig. 6d). These results imply that mineralized bone matrix not only reduces tumor cell proliferation *in vitro*, but also *in vivo*.

To evaluate the clinical relevance of our findings, we examined whether the gene expression signature induced by culturing tumor cells on mineralized vs. control collagen was predictive of patient survival. Indeed, upregulation of mineral-induced genes were associated with better patient prognosis in the METABRIC and TCGA cohorts consistent with our *in vitro* findings that matrix mineralization induces a more latent, less proliferative phenotype (Fig. 6e) and that tumor cells implanted on DCDM scaffolds grew more than their counterparts implanted on DC scaffolds. Analysis of cancer subtypes additionally showed that patients with luminal breast cancer, whose tumors primarily metastasize to bone, benefitted from upregulation of the mineral-induced gene signature whereas this was not the case for patients with basal breast cancer whose cancers preferentially metastasize to visceral organs (Supplementary Fig. 6)[53]. While this analysis used primary tumor specimens rather than specimens collected from bone metastatic tumors, these

bioRxiv preprint doi: https://doi.org/10.1101/2022.06.29.498001; this version posted July 2, 2022. The copyright holder for this preprint (which was not certified by peer review) is the author/funder. All rights reserved. No reuse allowed without permission.

results suggest that gene expression profiles induced by mineralized bone matrix correlate with increased patient survival possibly by selecting for less proliferative phenotypes. More broadly, these results indicate that bone matrix is a critical factor in regulating breast cancer cell fate *in vivo* with potential implications on the phenotype of tumor cells seeding osteogenic niches within the skeleton in human patients.

Discussion

Disseminating tumor cells target osteogenic niches within the skeleton[9,10] but how mineralization of collagen type-I, a hallmark of new bone formation, regulates the phenotype of breast cancer cells remains unexplored. Our results suggest that physiological collagen mineralization induces a less proliferative, more stem-like, phenotype in breast cancer cells while perturbed mineralization activates tumor cells to proliferate and form larger tumors (Fig. 6f). Moreover, these findings could help explain why breast cancer patients with decreased bone mineral density have a higher risk of developing bone metastasis[12,24].

Although ECM is known to regulate various aspects of breast cancer including metastasis,[54,55] its role in bone metastasis is less clear as studies in the skeleton are hindered by limited imaging modalities and difficulty of analyzing cells in this context. *In vitro* models can circumvent some of these limitations by allowing control over bone ECM materials properties. Here, we used biofunctional materials systems incorporating the basic building blocks of native bone ECM, hydroxyapatite-reinforced collagen fibrils[16,56]. With these models we were able to mimic defining materials properties of bone ECM across multiple lengths scales including bone hierarchical structure, ultrastructural arrangement, mineral-to-matrix ratio, and mineral crystallinity. Leveraging these models, we found that physiological collagen mineralization suppresses cancer

bioRxiv preprint doi: https://doi.org/10.1101/2022.06.29.498001; this version posted July 2, 2022. The copyright holder for this preprint (which was not certified by peer review) is the author/funder. All rights reserved. No reuse allowed without permission.

cell proliferation *in vitro* and tumor growth *in vivo*, and that mineral-induced changes in tumor stem-like properties may play a role in this process. These results suggest that physiological collagen mineralization may induce quiescence in breast cancer cells that have disseminated to osteogenic niches in the skeleton, giving new context to previous results showing that tumor cells assume a more stem-like phenotype following bone colonization[43].

While matrix mechanical properties are widely accepted to affect tumorigenesis, the effect of bone matrix mineralization on tumor cell mechanosignaling is poorly understood due in part to a lack of model systems that mimic the viscoelastic properties of bone more appropriately than the linearly elastic substrates that are routinely used for mechanosignaling studies. Collagen type I, the primary organic bone matrix component, exhibits non-linear elasticity and viscoelasticity[57]. Both properties can affect cell behavior[19] but are also impacted by mineralization[17]. More specifically, tumor cells can activate and reinforce mechanosignaling by strain-stiffening collagen[33], but collagen mineralization reduces this process[18]. On the other hand, stress relaxation occurs more slowly in mineralized collagen than collagen[18]. Our data suggest that these changes have functional consequences as cancer cells exert lower traction forces following interactions with mineralized versus non-mineralized collagen. These variations in traction forces manifested in a lack of response to pharmacological inhibitors of key nodes of mechanotransduction and correlated with reduced traction forces in more stem-like GFP^{high} versus GFP^{low} cells. Importantly, this correlation extended to an induction of phenotypic changes including upregulation of stem cell markers and functions, reduced cell proliferation, and increased anchorage-independent survival.

Our findings contradict the conventional assumption that bone stimulates malignancy by increasing mechanosignaling due to its increased rigidity and underline the importance of choosing

bioRxiv preprint doi: https://doi.org/10.1101/2022.06.29.498001; this version posted July 2, 2022. The copyright holder for this preprint (which was not certified by peer review) is the author/funder. All rights reserved. No reuse allowed without permission.

the correct materials system for mechanistic studies of tumor-ECM interactions. However, future studies will need to elucidate how mineralization-dependent changes of tumor cell phenotype affect other signaling mechanisms. For example, tumor cells can deposit and respond to their own matrix[58] and altered cell-ECM interactions can simultaneously regulate cellular responses to soluble factors. Integrins, for example, affect transforming growth factor -β (TGF-β) signaling via receptor cross-talk[59], a process that has been shown to modulate bone metastatic progression[13,60]. How mineralization-dependent changes in mechanosignaling and thus, integrin signaling may impact these mechanisms is unclear but warrants further investigation. Furthermore, many other cell types residing in the skeleton can respond to bone matrix changes and/or the bone matrix-dependent variations of tumor cell phenotype (e.g. endothelial cells, mesenchymal stromal cells, osteocytes, immune cells)[10,13,61,62]. Future studies will need to increase the complexity of the described culture models to consider their regulatory impact on the early stages of bone metastasis.

While we have validated the *in vivo* relevance of our findings with animal studies and with computational analysis of patient data, the model systems described herein should be further optimized for studies of mineral-dependent patient responses in a precision medicine setting. For example, the decellularized bone scaffolds utilized here were derived from neonatal bovine bone. The biomechanical properties of human bone and collagen are conserved between species, but it is likely that additional parameters influence bone matrix properties and thus, cancer cell response to mineralization. For example, age, gender, lifestyle, and prior treatment with chemotherapy are known regulators of bone material properties and health[21,22,25,39,63]. Future studies using bone specimens harvested from patients will help evaluate these connections and could be combined with matched organoid cultures rather than cell lines to directly test patient-specific responses to bone matrix properties. Furthermore, bone mineralization is a dynamic process, and it is possible

bioRxiv preprint doi: https://doi.org/10.1101/2022.06.29.498001; this version posted July 2, 2022. The copyright holder for this preprint (which was not certified by peer review) is the author/funder. All rights reserved. No reuse allowed without permission.

that tumor cell response is dependent on the time scales at which this process occurs. The mineralized substrates utilized here were prefabricated before seeding cells, but it is also possible to mineralize collagen *in situ*[62]. Finally, the flank implantation model we utilized here allowed for precise control of bone matrix mineral content independent of other parameters, which is not readily possible in the skeleton itself. Biomaterials scaffolds can influence tumor growth and metastasis by altering the recruitment of immune and other stromal cells[64,65], and while we observed infiltration by resident cells, the mineral-induced less proliferative tumor cell phenotype was maintained. How the phenotype of recruited cells may change in response to matrix mineral content and how such changes may regulate tumor cell phenotype will need to be considered in future work.

In conclusion, our findings suggest that changes in bone matrix properties are not only a consequence of osteolytic degradation during late-stage metastasis, but also a critical component dictating the early-stage development of bone metastases. These results are potentially of key clinical relevance as they could be used to inform future therapies that maintain cells in their quiescent state to prevent metastatic outgrowth. The finding that bone matrix mineral content inhibits breast cancer outgrowth motivates the clinical use of methods to increase or maintain physiological bone matrix mineralization, for example, by therapies that promote bone formation in settings of mechanical loading/exercise. Bisphosphonates are an alternative strategy to maintain bone mineral density and are routinely used as adjuvant therapy for breast cancer patients to reduce skeletal-related events and hypercalcemia. However, these drugs are only partially effective in preventing bone metastasis[66,67]. As bisphosphonates primarily prevent bone resorption rather than encourage new bone formation and thus, matrix mineralization, our results could help explain the limited success of bisphosphonates in prevention settings. Collectively, our results motivate a more

bioRxiv preprint doi: https://doi.org/10.1101/2022.06.29.498001; this version posted July 2, 2022. The copyright holder for this preprint (which was not certified by peer review) is the author/funder. All rights reserved. No reuse allowed without permission.

wholistic approach to modeling the bone ECM in future studies of bone metastasis and could yield insights that advance treatment options for breast cancer patients with advanced disease.

Methods

Fabrication of mineralized collagen. Mineralized collagen substrates for cell culture were fabricated using an adapted polymer-induced liquid-precursor (PILP) process (Fig. 1c) as previously described[18,31]. Briefly, poly(dimethylsiloxane) (PDMS) (Dow Corning, US) microwells (diameter: 4 mm, height: 250 µm) were prepared on a circular 8 mm PDMS base to enable flotation during mineralization. PDMS was then surface treated with 1% polyethyleneimine (PEI) (Sigma-Aldrich, US) and 0.1% glutaraldehyde (GA) (Thermo Fisher Scientific, US) to allow for covalent binding of pH-adjusted rat tail collagen, type I (Corning, US) (1.5 mg/mL). Mineralization was accomplished using a solution of 62.5 mg/mL of polyaspartic acid (PAA) (MW = 27 k Da, Alamanda Polymers, US), 1.67 mM $CaCl_2$ (Thermo Fisher Scientific, US) and 1 mM $(NH_4)_2HPO_4$ (Sigma-Aldrich, US) in 0.85 × phosphate buffered saline (PBS). To prevent precipitation of mineral on top rather than within collagen fibrils, substrates were incubated in the mineralization solution upside down using a humidified chamber for 1 day at 37 °C. Collagen control substrates were fabricated similarly, but immersed in PBS solution rather than mineralization solution. To adjust mineral content via controlled dissolution, fully mineralized collagen was incubated in 20 mM HEPES buffer (pH = 7.4) at ambient temperature for up to 6 days, changing HEPES buffer every 12 h.

Characterization of mineralized collagen. For characterization, collagen substrates were prepared on PEI/GA treated 8 mm diameter glass coverslips adhered to a PDMS base. SEM (Mira3 LM, Tescan, Czech Republic) visualized fiber morphology and confirmed mineral formation using

bioRxiv preprint doi: https://doi.org/10.1101/2022.06.29.498001; this version posted July 2, 2022. The copyright holder for this preprint (which was not certified by peer review) is the author/funder. All rights reserved. No reuse allowed without permission.

secondary electron (SEM) and backscattered electron (BSE) imaging modes. To this end, samples were dehydrated with a series of ethanol solutions and hexamethyldisiloxane and then carbon-coated (Desk II, Denton Vacuum, US). Changes in collagen fibril diameter were analyzed using the diameterJ function in ImageJ (NIH). Presence of mineral was detected by pseudocolor processing of BSE images using MATLAB (MathWorks, US). Mineral formation was also confirmed by Fourier transform infrared (FT-IR) spectrometry (Hyperion 2000/Tensor 27, Bruker, US). Samples were pelleted with potassium bromide (Thermo Fisher Scientific, US) and scanned in the range of 400 - 2000 cm^{-1}. Mineral to matrix ratio was determined by calculating the ratio of phosphate peak area (907 - 1183 cm^{-1}) and collagen amide I peak area (1580 - 1727 cm^{-1}) after correcting the FT-IR spectra base line using spectroscopy software (OPUS, Bruker, US). The crystallinity index of mineral (CI; CI= $(A_{567} + A_{603})/A_{590}$, where A*x* is the absorbance at wave number *x*) was determined using phosphate band splitting (See supplementary Fig. 1 and 3c). The phase of the formed mineral was determined using a powder X-ray diffractometer (XRD) (D8 advance ECO powder diffractometer, Bruker, US). Dried samples were mounted on a polymethyl methacrylate specimen holder and scanned in the range $2\theta = 15 - 45°$ with a step size of 0.0195 degrees and Cu Ka radiation ($\lambda = 1.54$ Å).

Cell culture and characterization of adhesion and proliferation. MDA-MB231 breast cancer cells (ATCC), MDA-MB231 expressing a Nanog-GFP reporter[44] (Nanog-GFP), bone metastatic BoM1-2287 (kindly provided by Joan Massague), and MCF-7 (ATCC) were routinely cultured in Minimum Essential Medium α (α-MEM) (Thermo Fisher Scientific, US) supplemented with 10% (v/v) fetal bovine serum (FBS) (Atlanta Biologicals, US) and 1% penicillin/streptomycin (P/S) (Thermo Fisher Scientific, US). Substrate-dependent differences of cell adhesion and growth were

bioRxiv preprint doi: https://doi.org/10.1101/2022.06.29.498001; this version posted July 2, 2022. The copyright holder for this preprint (which was not certified by peer review) is the author/funder. All rights reserved. No reuse allowed without permission.

determined by fluorescence analysis of DNA content with the QuantiFluor dsDNA kit (Promega, US) after 5 h and 7 d of culture, respectively. For analysis of cell morphology after 5 h of adhesion, cells were fixed with 10% formaldehyde and stained with DAPI (Invitrogen, US) and Alexa Fluor 568 phalloidin (Thermo Fisher Scientific, US). Confocal images (710 LSM, Zeiss, Germany) were captured with a 40× water immersion objective at 2 µm step size. Collagen structure was imaged in reflectance mode using a 488 nm laser. Cell proliferation was measured after 4 days using a BrdU staining kit (Life Biotechnologies, US) according to manufacturer's instructions. Images from six randomly selected areas per sample (n = 3) were captured with an epifluorescence microscope and BrdU positive cells were quantified using ImageJ.

Analysis of stem-like tumor cell phenotype. To validate the Nanog-GFP reporter cell line, cells were sorted into GFP^{high} and GFP^{low} populations using FACS. Sorted cells were lysed with RIPA buffer containing protease and phosphatase inhibitors (Thermo Fisher Scientific, US) and 1 mM phenylmethylsulfonyl fluoride (Calbiochem, US). All samples with equal amounts of protein were loaded on gels and separated by reducing SDS-PAGE and transferred to PVDF membranes (Bio-Rad, US). Membranes were blocked with 5% milk powder and incubated with rabbit anti-human Sox2 (Sigma Aldrich, US), rabbit anti-human Oct4 (Millipore, US), and rabbit anti-human HSP90 (Santa Cruz, US) overnight. Primary antibodies were detected by a horseradish peroxidase (HRP)-conjugated anti-rabbit antibody using an ECL kit (Thermo fisher Scientific, US) and imaged using ChemiDoc TM Touch Imaging System (Bio-Rad, US). Captured images were analyzed with Image Lab software (Bio-Rad, US). For analysis of matrix effect on GFP expression, Nanog-GFP cells were cultured on the different matrices and GFP levels per cell were analyzed from confocal images using the threshold tool in ImageJ. For flow cytometry Nanog-GFP cells cultured on tissue

bioRxiv preprint doi: https://doi.org/10.1101/2022.06.29.498001; this version posted July 2, 2022. The copyright holder for this preprint (which was not certified by peer review) is the author/funder. All rights reserved. No reuse allowed without permission.

culture polystyrene (PS) were trypsinized, while cells cultured on collagen and mineralized collagen were isolated using collagenase, Type I (1 mg/mL in PBS, Worthington Biochemical, US). Suspended cells were passed through a 40 µm cell strainer, centrifuged, and resuspended in flow cytometry buffer containing propidium iodide (PI) (Invitrogen, US) for subsequent flow cytometry (BD Accuri C6 Plus, BD biosciences, US). Aldehyde dehydrogenase (ALDH) activity of cells was measured using an ALDEFLUOR kit (StemCell Technologies, US) according to manufacturer's instructions. Cells were gated by FSC and SSC, then FSC-A and FSC-H signals were used for doublet exclusion. Live cells selected based on PI signals were used to identify cell populations expressing GFP from Nanog-GFP and ALDH from MDA-MB231. To analyze colony formation in soft agar, cells isolated from the different matrices (5×10^4 cells) were suspended in a solution of 0.3% noble agar in Dulbecco's Modified Eagle Medium (DMEM) with 10% FBS and 1% P/S and then plated on a layer of 0.5% noble agar in 6-well plates. After gelation, the plate was cultured in DMEM with 10% FBS and 1% P/S. After 21 days, cultures were incubated with media containing nitroblue tetrazolium (Biotium, US) overnight. Sphere formation was visualized using a ChemiDoc Touch Imaging System (Bio-Rad, US) and analyzed using the ImageJ particle analysis tool. Colonies over 100 µm of diameter were counted and measured for colony diameter distribution.

Analysis of mechanosignaling-mediated changes of cell growth. For analysis of mineralization-dependent changes of mechanosignaling, MDA-MB231 cells were cultured on PS, collagen and mineralized collagen in the presence and absence of a function-blocking β1 integrin antibody (2 µg/mL, Millipore, US) or pharmacological inhibitors of focal adhesion kinase (FAK) (FAK inhibitor 14, 5 µM, Tocris, UK), Rho-associated protein kinase (ROCK) (Y-27632, 25 µM, Tocris,

bioRxiv preprint doi: https://doi.org/10.1101/2022.06.29.498001; this version posted July 2, 2022. The copyright holder for this preprint (which was not certified by peer review) is the author/funder. All rights reserved. No reuse allowed without permission.

UK), or phosphoinositide 3-kinase (PI3K) (LY 294002, 10 µM, Tocris, UK) for 4 days. Subsequently, cell growth was analyzed by measuring DNA content as described above.

Analysis of cell traction forces. Polyacrylamide gels were prepared with a Young's modulus of either 2.7 kPa for Nanog-GFP and 5 kPa for MDA-MB231 cells as previously described[68]. Briefly, 35 mm glass-bottom dishes (VWR, US) were cleaned with 0.1 N NaOH, followed by sequential surface treatment with 3-aminopropyl-trimethylsilane and 0.5% (v/v) glutaraldehyde in PBS. Dishes were washed with distilled water (dH_2O) and allowed to air dry. Prepolymer solutions for gels were prepared by combining 40% acrylamide, 2% bisacrylamide, PBS, and 0.2 µm fluorescent beads (Thermo Fisher Scientific, US). 2.7 kPa and 5 kPa gels were prepared using 7.5%/0.035% and 7.5%/0.06% of acrylamide/bisacrylamide, respectively. Polymerization was initiated through the addition of ammonium persulfate and N,N,N,N-tetramethyl ethylenediamine. Droplets of the polymer solution were placed between activated dishes and a Sigmacote®-treated 8 mm coverslip (Sigma-Aldrich, US), and allowed to polymerize. Polyacrylamide gels were functionalized with rat tail type-I collagen (0.03 mg/mL) using an N6 succinimide ester crosslinker solution as previously described[69]. Gels were washed with PBS and cell media prior to cell seeding at 1×10^3 cells/cm^2.

Confocal microscopy (810 and 880 LSM, Zeiss, Germany) was used to image Nanog-GFP or MemGlow 590 (20 nM, Cytoskeleton, US) labeled MDA-MB231 cells using either 63× or 40×, 1.2NA C-Apochromat objectives. Cells were lysed by adding 2% sodium dodecyl-sulfate (SDS) to the dishes (final concentration of 1% SDS) and gels allowed to relax for 2 min. Images of the relaxed gels were then acquired at the same positions. Images of beads were sharpened, and stage drift corrected using ImageJ, and bead displacements and corresponding forces calculated using

bioRxiv preprint doi: https://doi.org/10.1101/2022.06.29.498001; this version posted July 2, 2022. The copyright holder for this preprint (which was not certified by peer review) is the author/funder. All rights reserved. No reuse allowed without permission.

previously developed software and custom MatLAB® scripts[70]. Cellular traction forces were calculated using the Fourier transform traction cytometry (FTTC) method with a regularization parameter (λ) of 1×10^{-9}. For MDA-MB231, traction forces of at least 12 cells were analyzed per gel for a minimum of 3 gels per condition. For Nanog-GFP, traction forces of at least 25 cells per condition were analyzed from 5 gels. Pairwise comparisons of total cellular traction forces were conducted using either a Mann-Whitney U-test or a Kruskal-Wallis test with Dunn's multiple comparison correction when more than two conditions were being compared. For cellular traction forces when cells were precultured on different substrates, outliers were identified using the ROUT method with a Q value of 1%.

RNA-sequencing (RNA-seq) and data analysis. Cells were collected using collagenase after 7 days of culture, and RNA was isolated from each condition using an RNA isolation kit (Qiagen, US) according to the manufacturer's protocols (n = 4). Illumina TruSeq RNA stranded kit (Illumina, US) was used for library preparation, and samples were sequenced as 1 × 86 bp single-end reads on the NextSeq500 (Illumina, US), yielding on average 42 M reads per sample. Reads were then trimmed using Trim Galore (version 0.4.4; https://www.bioinformatics.babraham.ac.uk/projects/trim_galore/), and aligned to the human reference genome GRCh38 (ENSEMBL) using STAR (version 2.6.0a)[71]. Reads of genomic features were counted using featureCounts[72], and differential gene expression determined using DESeq2[73]. Differentially expressed genes were defined as those with a $\log_2$-fold change greater than |1| and an adjusted p-value less than 0.05. For gene set enrichment analysis (GSEA), a ranked list was generated by taking the sign of the fold change multiplied by the $-\log_{10}$ of the adjusted p-value. The list was inputted to the GSEA Java applet

bioRxiv preprint doi: https://doi.org/10.1101/2022.06.29.498001; this version posted July 2, 2022. The copyright holder for this preprint (which was not certified by peer review) is the author/funder. All rights reserved. No reuse allowed without permission.

(http://software.broadinstitute.org/gsea/index.jsp) using gene ontology biological processes gene sets from MSigDB v.6.2. Gene sets were considered significantly enriched with a p-value and FDR value < 0.05.

The relevance of gene expression changes induced by mineralized collagen to human breast cancer samples was computed using publicly available TCGA and METABRIC datasets. The 98-gene mineralized collagen gene signature was defined as transcripts with a $\log_2$-Fold Change ≥ 1 and a p-adjusted value ≤ 0.05. The transcriptional score based on supervised gene signature was computed across all samples using the Single Sample Gene Set Enrichment Analysis method (SSGSEA) from the *gsva* package. SSGSEA scores were utilized for clinical correlations with survival. In TCGA and METABRIC cohorts, sorted signature scores in the upper and lower tertiles were classified as high and low transcriptional signature, respectively. Kaplan-Meier survival analysis was then performed using coxph regression using the *survival* package in R to associate transcriptional signature score with overall survival as primary outcome.

Preparation and characterization of bone scaffolds. Trabecular bone biopsies were extracted from 1-3 day-old neonatal bovine distal femurs as previously described[50]. After rinsing with a high velocity stream of deionized water to remove marrow and debris, biopsies were sectioned into cylindrical scaffolds (6 mm-diameter and 1 mm-thickness). Scaffolds were incubated in an extraction buffer of 20 mM NaOH and 0.5% Triton X-100 in PBS at 37 °C to remove cells and cellular debris, then incubated in 20 U/mL DNase I to remove any latent DNA fragments (decellularized [DC] scaffolds). Bone mineral was removed from DC scaffolds with an overnight incubation in 9.5% ethylenediaminetetraacetic acid (EDTA) (decellularized and demineralized [DCDM] scaffolds). All scaffolds were then washed 5 times with PBS to clear any residual

bioRxiv preprint doi: https://doi.org/10.1101/2022.06.29.498001; this version posted July 2, 2022. The copyright holder for this preprint (which was not certified by peer review) is the author/funder. All rights reserved. No reuse allowed without permission.

material. Removal of cellular components was confirmed by H&E staining as well as DNA quantification. To confirm demineralization, scaffolds were scanned on a high resolution 3D X-ray microscope (Xradia Zeiss Versa XRM-520, Zeiss, Germany) at 60 kV/5W, with exposures of 1.5 seconds each, at a resolution of 3.53 microns/pixel, and false-colored based on the attenuation coefficient (Avizo, Thermo Fisher Scientific, US). To assess collagen content, Masson's trichrome staining was performed on formalin fixed, paraffin-embedded sections according to standard protocols. Trabecular structure and collagen microstructure of DC and DCDM scaffolds were measured by SEM and second harmonic generation (SHG) microscopy, respectively. XRD and FT-IR spectra were used to characterize mineral properties of scaffolds as described above. For detection of cell growth, MDA-MB231 cells were imaged by SEM and quantified by fluorescence analysis of DNA content with the QuantiFluor dsDNA kit (Promega, US). For detection of stem-like properties of cells in scaffolds, GFP expression of Nanog-GFP was imaged by confocal microscopy and quantified using flow cytometry.

Animal Studies. Mouse studies were performed in accordance with Cornell University animal care guidelines and was approved by Cornell University's Institutional Animal Care and Use Committee (IACUC). For detection of disseminated tumor cells relative to mineralizing bone surfaces, MDA-MB231 cells were labeled with fluorescent silica nanoparticles containing positively charged Cy5 dye (Cy5(+)-SNPs) as previously described[29]. Briefly, cells were labeled with 1 μM Cy5(+)-SNPs and resuspended in ice-cold PBS for mouse injections. Female athymic nude-Foxn1nu (Envigo, US) mice were injected intraperitoneally with calcein (15 mg/kg, pH 7.4 in PBS) at 5-6 weeks of age. One day later, labeled cells (1×10^5 cells in 100 μL PBS) were injected into the left cardiac ventricle using ultrasound guidance (Vevo VisualSonics 2100,

bioRxiv preprint doi: https://doi.org/10.1101/2022.06.29.498001; this version posted July 2, 2022. The copyright holder for this preprint (which was not certified by peer review) is the author/funder. All rights reserved. No reuse allowed without permission.

FUJIFILM VisualSonics, Canada). Injection into the systemic circulation was verified by bioluminescence imaging (IVIS Spectrum, Perkin Elmer, US). Tibiae were harvested after 2 days. Immediately following harvest, tibiae were fixed in ice-cold 4% paraformaldehyde (pH 7.4 in PBS) for 16 h. To detect tumor cells labeled with Cy5(+)-SNPs, tibiae were optically cleared using ethyl cinnamate following dehydration in a graded ethanol series[74]. Samples were imaged in ethyl cinnamate using a light sheet microscope (LaVision BioTec, Germany), using the 488 nm laser to detect calcein and the 640 nm laser to detect Cy5(+)-SNPs. Arivis Vision4D (Arivis, Germany) and ImageJ were used to process light sheet microscopy images.

For *in vivo* tumor formation, luciferase-expressing MDA-MB231 were seeded on bovine bone scaffolds (6 mm-diameter and 1 mm-thickness) in α-MEM with 10% FBS and 1% P/S (4×10^5 cells/scaffold) and cultured at 37 °C in a 5% CO_2 incubator for 24 h prior to implantation. Cell-laden scaffolds (decellularized [DC] vs decellularized and demineralized [DCDM]) were implanted subcutaneously into six- to eight-week-old female BALB/c athymic nude mice (Taconic Biosciences, US). Two scaffolds per condition were implanted into each mouse (*i.e.*, 4 scaffolds per mouse; n=4 mice; 8 scaffolds per condition). Bioluminescence images were taken once weekly 5 min following injection of D-luciferin (Gold Biotechnology, US) with an in vivo imaging system (IVIS Spectrum, Perkin Elmer, US). Outliers were determined using a Grubb's test with a significance level of alpha = 0.0001. Explanted scaffolds were fixed with ice-cold 4% paraformaldehyde and decalcified with 10% EDTA. Paraffin sections were used for H&E staining as well as sequential double-immuno-staining with rabbit anti-human Ki67 (Cell Signaling Technologies, US) and rabbit anti-human vimentin (Thermo Fisher Scientific, US). First, Ki67 antibody was detected with an alkaline phosphatase (AP)-conjugated horse anti-rabbit antibody to stain red following incubation with AP substrate (Vector Laboratories, US). After blocking Ki67-

bioRxiv preprint doi: https://doi.org/10.1101/2022.06.29.498001; this version posted July 2, 2022. The copyright holder for this preprint (which was not certified by peer review) is the author/funder. All rights reserved. No reuse allowed without permission.

stained samples with horse serum, human vimentin antibody was detected with a HRP-conjugated horse anti-rabbit antibody and diaminobenzidine (DAB) to produce a brown color (Thermo Fisher Scientific, US). All sections were counterstained with Mayer's hematoxylin (Thermo Fisher Scientific, US) and imaged using a ScanScope slide scanner (Aperio CS2, Leica Biosystems, Germany) with a 40× objective. To quantify Ki67 and vimentin immunoreactivity, images of all IHC-stained sections were uploaded to QuPath v0.2.0[75] and manually annotated to include cells and exclude trabeculae, lipid deposits, and extracellular debris. A QuPath script was written to quantify the total number of cells, total section area, and number of cells positive for vimentin and Ki67 per section area. Each data point represents the percentage of positive cells per mm^2 as identified for the cross-sectional area of 1 implant; 8 implants were analyzed per condition.

Statistical analysis. Unless otherwise indicated results are presented as the mean and standard deviation (SD) of at least 3 independent replicates per condition using Prism 8 software (GraphPad, US). Statistical differences were determined by Student's unpaired *t*-test for two group comparisons, one-way analysis of variance (ANOVA) followed by Tukey's post test for multiple group comparisons and two-way ANOVA with Sidak's multiple comparison for multiple factors, unless otherwise mentioned. Two-tailed test with $P < 0.05$ were considered significant in all cases. Statistical considerations for analysis of cell traction forces and tumor growth *in vivo* are specified in the respective sections above.

Acknowledgements

We thank all members of the Fischbach lab for valuable discussions of this research, the Wiesner group for providing fluorescent silica nanoparticles, Joe Kuo for help with illustrations, Lauren

bioRxiv preprint doi: https://doi.org/10.1101/2022.06.29.498001; this version posted July 2, 2022. The copyright holder for this preprint (which was not certified by peer review) is the author/funder. All rights reserved. No reuse allowed without permission.

O'Keeffe for help with preparation of bone scaffolds, the Cornell Animal Health Diagnostic Core for paraffin embedding and sectioning, and the Cornell Center for Animal Resources and Education (CARE) staff for animal care. Financial support was provided by the Human Frontier Science Program (RGP0016/2017), the National Cancer Institute through the Center on the Physics of Cancer Metabolism (1U54CA210184), and NSF GRFP to M.A.W and A.A.S. (DGE-1650441). This work utilized the Cornell Center for Materials Research (CCMR), which is supported through the NSF MRSEC program (DMR-1719875), the Cornell NanoScale Science & Technology Facility (CNF), a member of the NSF-supported National Nanotechnology Coordinated Infrastructure (NNCI-2025233), and the Cornell University Biotechnology Resource Center (BRC) facilities, including Zeiss LSM 710 Confocal Microscope (NIH 1S10RR025502), Zeiss LSM880 confocal/multiphoton microscope (NYSTEM (C029155) and NIH (S10OD018516)), light sheet microscope (NIH S10OD023466), ZEISS/Xradia Versa 520 X-ray Microscope (NIH S10OD012287), IVIS Spectrum (NIH S10OD025049), and Genomics Facility (RRID:SCR_021727).

Author contributions

S.C., M.A.W., L.A.E. and C.F. designed the project. S.C. and M.A.W. conducted most of the experiments. A.A.S. performed and analyzed FACS and RNA-seq. A.C. performed the animal study for light sheet microscopy. J.D. performed FACS. A.V. and O.E. analyzed RNA-seq data with SSGSEA method. S.L analyzed IHC images. Z.C, A.A.S., and M.P. conducted and analyzed TFM. S.C., M.A.W., L.A.E. and C.F. analyzed the data and wrote manuscript. All authors discussed the results and commented on the manuscript.

bioRxiv preprint doi: https://doi.org/10.1101/2022.06.29.498001; this version posted July 2, 2022. The copyright holder for this preprint (which was not certified by peer review) is the author/funder. All rights reserved. No reuse allowed without permission.

Competing interests

OE is supported by Janssen, J&J, Astra-Zeneca, Volastra and Eli Lilly research grants. He is scientific advisor and equity holder in Freenome, Owkin, Volastra Therapeutics and One Three Biotech and a paid scientific advisor to Champions Oncology and Pionyr Therapeutics.

Data availability

The main data supporting the results in this study are available within the paper and its Supplementary Information. All RNA sequence data generated in this study are available from the corresponding author upon reasonable request. Source data for the figures are provided with this paper.

Code availability

QuPath script is available from the corresponding author upon request.

bioRxiv preprint doi: https://doi.org/10.1101/2022.06.29.498001; this version posted July 2, 2022. The copyright holder for this preprint (which was not certified by peer review) is the author/funder. All rights reserved. No reuse allowed without permission.

References

1. Hess, K. R. et al. Metastatic patterns in adenocarcinoma. *Cancer* **106**, 1624–1633 (2006).

2. Kuchuk, I. et al. Incidence, consequences and treatment of bone metastases in breast cancer patients—Experience from a single cancer centre. *Journal of Bone Oncology* **2**, 137–144 (2013).

3. Braun, S. et al. A Pooled Analysis of Bone Marrow Micrometastasis in Breast Cancer. *New England Journal of Medicine* **353**, 793–802 (2005).

4. Guise, T. A. & Guise, T. A. The vicious cycle of bone metastases. *J. Musculoskelet Neuronal Interact* **2**, 570–572 (2002).

5. Lawson, M. A. et al. Osteoclasts control reactivation of dormant myeloma cells by remodelling the endosteal niche. *Nature Communications* **6**, 9983 (2015).

6. Hüsemann, Y. et al. Systemic Spread Is an Early Step in Breast Cancer. *Cancer Cell* **13**, 58–68 (2008).

7. Sosa, M. S., Bragado, P. & Aguirre-Ghiso, J. A. Mechanisms of disseminated cancer cell dormancy: An awakening field. *Nature Reviews Cancer* **14**, 611–622 (2014).

8. Risson, E., Nobre, A. R., Maguer-Satta, V. & Aguirre-Ghiso, J. A. The current paradigm and challenges ahead for the dormancy of disseminated tumor cells. *Nature Cancer* **1**, 672–680 (2020).

9. Wang, H. et al. The Osteogenic Niche Promotes Early-Stage Bone Colonization of Disseminated Breast Cancer Cells. *Cancer Cell* **27**, 193–210 (2015).

10. Croucher, P. I., McDonald, M. M. & Martin, T. J. Bone metastasis: The importance of the neighbourhood. *Nature Reviews Cancer* **16**, 373–386 (2016).

11. Luo, X. et al. Stromal-Initiated Changes in the Bone Promote Metastatic Niche Development. *Cell Reports* **14**, 82–92 (2016).

12. Yao, Z. et al. Therapy-induced senescence drives bone loss. *Cancer Research* **80**, 1171–1182 (2020).

13. Nobre, A. R. et al. Bone marrow NG2+/Nestin+ mesenchymal stem cells drive DTC dormancy via TGF-β2. *Nature Cancer* **2**, 327–339 (2021).

14. Andersen, T. L. et al. A physical mechanism for coupling bone resorption and formation in adult human bone. *American Journal of Pathology* **174**, 239–247 (2009).

15. Blair, H. C. et al. Osteoblast differentiation and bone matrix formation in vivo and in vitro. *Tissue Engineering - Part B: Reviews* **23**, 268–280 (2017).

16. Reznikov, N., Bilton, M., Lari, L., Stevens, M. M. & Kröger, R. Fractal-like hierarchical organization of bone begins at the nanoscale. *Science* **360**, eaao2189 (2018).

17. Ping, H. et al. Mineralization generates megapascal contractile stresses in collagen fibrils. *Science* **376**, 188–192 (2022).

18. Choi, S. et al. Intrafibrillar, bone-mimetic collagen mineralization regulates breast cancer cell adhesion and migration. *Biomaterials* **198**, 95–106 (2019).

bioRxiv preprint doi: https://doi.org/10.1101/2022.06.29.498001; this version posted July 2, 2022. The copyright holder for this preprint (which was not certified by peer review) is the author/funder. All rights reserved. No reuse allowed without permission.

19. Chaudhuri, O., Cooper-White, J., Janmey, P. A., Mooney, D. J. & Shenoy, V. B. Effects of extracellular matrix viscoelasticity on cellular behaviour. *Nature* **584**, 535–546 (2020).

20. Paschalis, E. P., Betts, F., DiCarlo, E., Mendelsohn, R. & Boskey, A. L. FTIR microspectroscopic analysis of normal human cortical and trabecular bone. *Calcified Tissue International* **61**, 480–486 (1997).

21. Turunen, M. J., Prantner, V., Jurvelin, J. S., Kröger, H. & Isaksson, H. Composition and microarchitecture of human trabecular bone change with age and differ between anatomical locations. *Bone* **54**, 118–125 (2013).

22. Donnelly, E., Boskey, A. L., Baker, S. P. & van der Meulen, M. C. H. Effects of tissue age on bone tissue material composition and nanomechanical properties in the rat cortex. *Journal of Biomedical Materials Research - Part A* **92**, 1048–1056 (2010).

23. Burke, M. V., Atkins, A., Akens, M., Willett, T. L. & Whyne, C. M. Osteolytic and mixed cancer metastasis modulates collagen and mineral parameters within rat vertebral bone matrix. *Journal of Orthopaedic Research* **34**, 2126–2136 (2016).

24. Mathis, K. M. et al. Bone resorption and bone metastasis risk. *Medical Hypotheses* **118**, 36–41 (2018).

25. Lynch, M. E. et al. In vivo tibial compression decreases osteolysis and tumor formation in a human metastatic breast cancer model. *Journal of Bone and Mineral Research* **28**, 2357–2367 (2013).

26. Swami, S. et al. Prevention of breast cancer skeletal metastases with parathyroid hormone. *JCI Insight* **2**, e90874 (2017).

27. Farr, J. N. et al. Targeting cellular senescence prevents age-related bone loss in mice. *Nature Medicine* **23**, 1072–1079 (2017).

28. Gower, L. & Elias, J. Colloid assembly and transformation (CAT): The relationship of PILP to biomineralization. *Journal of Structural Biology: X* **6**, 100059 (2022).

29. Chiou, A. E. et al. Fluorescent Silica Nanoparticles to Label Metastatic Tumor Cells in Mineralized Bone Microenvironments. *Small* **17**, 2001432 (2021).

30. Carlson, P. et al. Targeting the perivascular niche sensitizes disseminated tumour cells to chemotherapy. *Nature Cell Biology* **21**, 238–250 (2019).

31. Olszta, M. J. et al. Bone structure and formation: A new perspective. *Materials Science and Engineering R: Reports* **58**, 77–116 (2007).

32. Londoño-Restrepo, S. M., Jeronimo-Cruz, R., Millán-Malo, B. M., Rivera-Muñoz, E. M. & Rodriguez-García, M. E. Effect of the Nano Crystal Size on the X-ray Diffraction Patterns of Biogenic Hydroxyapatite from Human, Bovine, and Porcine Bones. *Scientific Reports* **9**, 5915 (2019).

33. Hall, M. S. et al. Fibrous nonlinear elasticity enables positive Mechanical feedback between cells and ECMs. *Proc. Natl. Acad. Sci. USA* **113**, 14043–14048 (2016).

bioRxiv preprint doi: https://doi.org/10.1101/2022.06.29.498001; this version posted July 2, 2022. The copyright holder for this preprint (which was not certified by peer review) is the author/funder. All rights reserved. No reuse allowed without permission.

34. Masuda, T. et al. ANGPTL2 increases bone metastasis of breast cancer cells through enhancing CXCR4 signaling. *Scientific Reports* **5**, 9170 (2015).

35. Bergamaschi, A. et al. CAMK1D amplification implicated in epithelial-mesenchymal transition in basal-like breast cancer. *Molecular Oncology* **2**, 327–339 (2008).

36. Dong, X., Yang, Y., Yuan, Q., Hou, J. & Wu, G. High Expression of CEMIP Correlates Poor Prognosis and the Tumur Microenvironment in Breast Cancer as a Promisingly Prognostic Biomarker. *Frontiers in Genetics* **12**, 768140 (2021).

37. Che, M. I. et al. β1, 4-N-acetylgalactosaminyltransferase III modulates cancer stemness through EGFR signaling pathway in colon cancer cells. *Oncotarget* **5**, 3673–3684 (2014).

38. Yu, J. M. et al. TRIB3 supports breast cancer stemness by suppressing FOXO1 degradation and enhancing SOX2 transcription. *Nature Communications* **10**, 5720 (2019).

39. Bruning, P. F. et al. Bone mineral density after adjuvant chemotherapy for premenopausal breast cancer. *British Journal of Cancer* **61**, 308–310 (1990).

40. Balestrini, J. L., Chaudhry, S., Sarrazy, V., Koehler, A. & Hinz, B. The mechanical memory of lung myofibroblasts. *Integrative Biology* **4**, 410–421 (2012).

41. Li, C. X. et al. MicroRNA-21 preserves the fibrotic mechanical memory of mesenchymal stem cells. *Nature Materials* **16**, 379–389 (2016).

42. Phan, T. G. & Croucher, P. I. The dormant cancer cell life cycle. *Nature Reviews Cancer* **20**, 398–411 (2020).

43. Zhang, W. et al. The bone microenvironment invigorates metastatic seeds for further dissemination. *Cell* **184**, 2471-2486 (2021).

44. Thiagarajan, P. S. et al. Development of a fluorescent reporter system to delineate cancer stem cells in triple-negative breast cancer. *Stem Cells* **33**, 2114–2125 (2015).

45. Ginestier, C. et al. ALDH1 Is a Marker of Normal and Malignant Human Mammary Stem Cells and a Predictor of Poor Clinical Outcome. *Cell Stem Cell* **1**, 555–567 (2007).

46. Raha, D. et al. The cancer stem cell marker aldehyde dehydrogenase is required to maintain a drug-tolerant tumor cell subpopulation. *Cancer Research* **74**, 3579–3590 (2014).

47. Paszek, M. J. et al. Tensional homeostasis and the malignant phenotype. *Cancer Cell* **8**, 241–254 (2005).

48. Seo, B. R. et al. Collagen microarchitecture mechanically controls myofibroblast differentiation. *Proc. Natl. Acad. Sci. USA* **117**, 11387-11398 (2020).

49. Reznikov, N. et al. Biological stenciling of mineralization in the skeleton: Local enzymatic removal of inhibitors in the extracellular matrix. *Bone* **138**, 115447 (2020).

50. Boys, A. J. et al. Top-Down Fabrication of Spatially Controlled Mineral-Gradient Scaffolds for Interfacial Tissue Engineering. *ACS Biomaterials Science and Engineering* **5**, 2988-2997 (2019).

bioRxiv preprint doi: https://doi.org/10.1101/2022.06.29.498001; this version posted July 2, 2022. The copyright holder for this preprint (which was not certified by peer review) is the author/funder. All rights reserved. No reuse allowed without permission.

51. Zhou, H., Boys, A. J., Harrod, J. B., Bonassar, L. J. & Estroff, L. A. Mineral Distribution Spatially Patterns Bone Marrow Stromal Cell Behavior on Monolithic Bone Scaffolds. *Acta Biomaterialia* **112**, 274–285 (2020).

52. Crapo, P. M., Gilbert, T. W. & Badylak, S. F. An overview of tissue and whole organ decellularization processes. *Biomaterials* **32**, 3233–3243 (2011).

53. Gao, Y. et al. Metastasis Organotropism: Redefining the Congenial Soil. *Developmental Cell* **49**, 375–391 (2019).

54. Cox, T. R. The matrix in cancer. *Nature Reviews Cancer* **21**, 217–238 (2021).

55. Reuten, R. et al. Basement membrane stiffness determines metastases formation. *Nature Materials* **20**, 892–903 (2021).

56. Fratzl, P., Gupta, H. S., Paschalis, E. P. & Roschger, P. Structure and mechanical quality of the collagen-mineral nano-composite in bone. *Journal of Materials Chemistry* **14**, 2115–2123 (2004).

57. Nam, S., Hu, K. H., Butte, M. J. & Chaudhuri, O. Strain-enhanced stress relaxation impacts nonlinear elasticity in collagen gels. *Proc. Natl. Acad. Sci. USA* **113**, 5492–5497 (2016).

58. Barney, L. E. *et al.* Tumor cell-organized fibronectin maintenance of a dormant breast cancer population. *Science Advances* **6**, eaaz4157 (2020).

59. Margadant, C. & Sonnenberg, A. Integrin-TGF-β crosstalk in fibrosis, cancer and wound healing. *EMBO Reports* **11**, 97–105 (2010).

60. Bragado, P. et al. TGF-β2 dictates disseminated tumour cell fate in target organs through TGF-β-RIII and p38α/β signalling. *Nature Cell Biology* **15**, 1351–1361 (2013).

61. Marturano-Kruik, A. *et al.* Human bone perivascular niche-on-a-chip for studying metastatic colonization. *Proc. Natl. Acad. Sci.* **115**, 1256–1261 (2018).

62. Thrivikraman, G. et al. Rapid fabrication of vascularized and innervated cell-laden bone models with biomimetic intrafibrillar collagen mineralization. *Nature Communications* **10**, 3520 (2019).

63. Boskey, A. L. & Coleman, R. Critical reviews in oral biology & medicine: Aging and bone. *Journal of Dental Research* **89**, 1333–1348 (2010).

64. Azarin, S. M. et al. In vivo capture and label-free detection of early metastatic cells. *Nature Communications* **6**, 8094 (2015).

65. Sadtler, K. et al. Divergent immune responses to synthetic and biological scaffolds. *Biomaterials* **192**, 405–415 (2019).

66. Early Breast Cancer Trialists' Collaborative Group (EBCTCG) Adjuvant bisphosphonate treatment in early breast cancer: Meta-analyses of individual patient data from randomised trials. *The Lancet* **386**, 1353–1361 (2015).

67. Coleman, R. E. et al. Breast-Cancer Adjuvant Therapy with Zoledronic Acid. *New England Journal of Medicine* **365**, 1396–1405 (2011).

68. Pelham, R. J. & Wang, Y. L. Cell locomotion and focal adhesions are regulated by substrate flexibility. *Proc. Natl. Acad. Sci. USA* **94**, 13661-13665 (1997).

bioRxiv preprint doi: https://doi.org/10.1101/2022.06.29.498001; this version posted July 2, 2022. The copyright holder for this preprint (which was not certified by peer review) is the author/funder. All rights reserved. No reuse allowed without permission.

69. Przybyla, L., Lakins, J. N., Sunyer, R., Trepat, X. & Weaver, V. M. Monitoring developmental force distributions in reconstituted embryonic epithelia. *Methods* **94**, 101–113 (2016).

70. Han, S. J., Oak, Y., Groisman, A. & Danuser, G. Traction microscopy to identify force modulation in subresolution adhesions. *Nature Methods* **12**, 653–656 (2015).

71. Dobin A. et al. STAR: ultrafast universal RNA-seq aligner. *Bioinformatics* **29,** 15-21 (2013).

72. Liao, Y., Smyth, G. K. & Shi, W. featureCounts: an efficient general purpose program for assigning sequence reads to genomic features. *Bioinformatics* **30**, 923–930 (2014).

73. Love, M. I., Huber, W. & Anders, S. Moderated estimation of fold change and dispersion for RNA-seq data with DESeq2. *Genome Biology* **15**, 550 (2014).

74. Grüneboom, A. et al. A network of trans-cortical capillaries as mainstay for blood circulation in long bones. *Nature Metabolism* **1**, 236–250 (2019).

75. Bankhead, P. et al. QuPath: Open source software for digital pathology image analysis. *Scientific Reports* **7**, 16878 (2017).

bioRxiv preprint doi: https://doi.org/10.1101/2022.06.29.498001; this version posted July 2, 2022. The copyright holder for this preprint (which was not certified by peer review) is the author/funder. All rights reserved. No reuse allowed without permission.

Table 1. Top 50 differentially expressed genes between collagen and mineralized collagen (p-value < 0.05)

Top 50 Ranked Genes			
Mineralized Collagen		**Collagen**	
ABCA3	NEDD9	AC006058.1	KIF23
ADM2	NNMT	AC008735.2	L3HYPDH
ANGPTL2	NUPR1	AC068831.7	LAPTM5
AQP1	PDLIM4	AHSA2P	LUC7L3
ATF3	PLAT	AJUBA	MAMDC4
B4GALNT3	PRSS2	AL136164.4	MAP7D3
BHLHE40	PRSS3	ALS2CL	MIR222HG
BMF	PTGS2	ARGLU1	MIR503HG
CAMK1D	RRAD	ARHGAP33	NSUN5P1
CEMIP	SELENOM	CARS2	PABPC1L
CHAC1	SGK1	CASP2	PLEKHA7
CRIP2	SLC43A2	CCDC14	PLK4
CTSF	SLFN5	CDCA7	PNISR
EPHB6	SMIM14	CDH24	PNN
FBN2	SQSTM1	CDK5RAP3	RAD54L
FOS	TAGLN2	CHTF18	RECQL4
FOSB	TCP11L2	CREBZF	RSRP1
HDAC5	TMEM45B	DBF4B	SEMA7A
IGFBP1	TPPP	DDX12P	SERINC2
KLHL24	TPPP3	DDX39B	SLC25A27
KRT19	TRIB3	FAM193B	SUGP2
LGALS3	TSC22D1	HJURP	TGM2
MEF2C	TSC22D3	IL11	TROAP
MRPL41	TYMP	KIF18B	VAMP1
NBL1	VWA1	KIF20A	ZNF692

bioRxiv preprint doi: https://doi.org/10.1101/2022.06.29.498001; this version posted July 2, 2022. The copyright holder for this preprint (which was not certified by peer review) is the author/funder. All rights reserved. No reuse allowed without permission.

Table 2. Gene signature of MDA-MB231 cultured on mineralized collagen.

Mineralized Collagen Gene Signature			
ABCG1	CHI3L2	LINC01607	SPINK4
ABHD11-AS1	CRIP2	LIPG	STEAP4
AC018816.1	CSF2	LRRK2	TCP11L2
AC024575.1	CSRP3	MEF2C	TFF1
AC026403.1	DEPP1	MUC12	TFF2
AC095055.1	DHRS9	NANOS3	TFF3
ACOT1	EGR3	NEURL1	TNFSF10
ADM2	EPHB6	NFE2	TPPP
AK8	FAM20A	NNMT	TPPP3
AL161787.1	FBN2	NR4A1	TRBC1
AL355312.3	FN1	NR4A2	TRBV30
AL356019.2	FOS	NUPR1	TRIB3
AP000808.1	FOSB	P2RX1	TRPV6
AQP1	FOXS1	PCDHGA7	TSC22D3
ATF3	GAS7	PHOSPHO1	TSPAN8
ATP6V0D2	GKN2	PRSS1	TYMP
B4GALNT2	HECW2-AS1	PRSS2	VLDLR-AS1
B4GALNT3	HPGD	PTGS2	VWA1
BMF	HSD3B1	PTHLH	WFDC10B
C4B	IGFL2-AS1	PTPRR	WFDC3
CA14	KLHL24	RRAD	ZBTB20
CD52	KLRC2	SERPINA5	ZDHHC11B
CDC42EP5	KPNA7	SGK1	ZNF474
CDHR5	KRT33B	SLC43A2	
CHAC1	LINC00607	SMIM1	

bioRxiv preprint doi: https://doi.org/10.1101/2022.06.29.498001; this version posted July 2, 2022. The copyright holder for this preprint (which was not certified by peer review) is the author/funder. All rights reserved. No reuse allowed without permission.

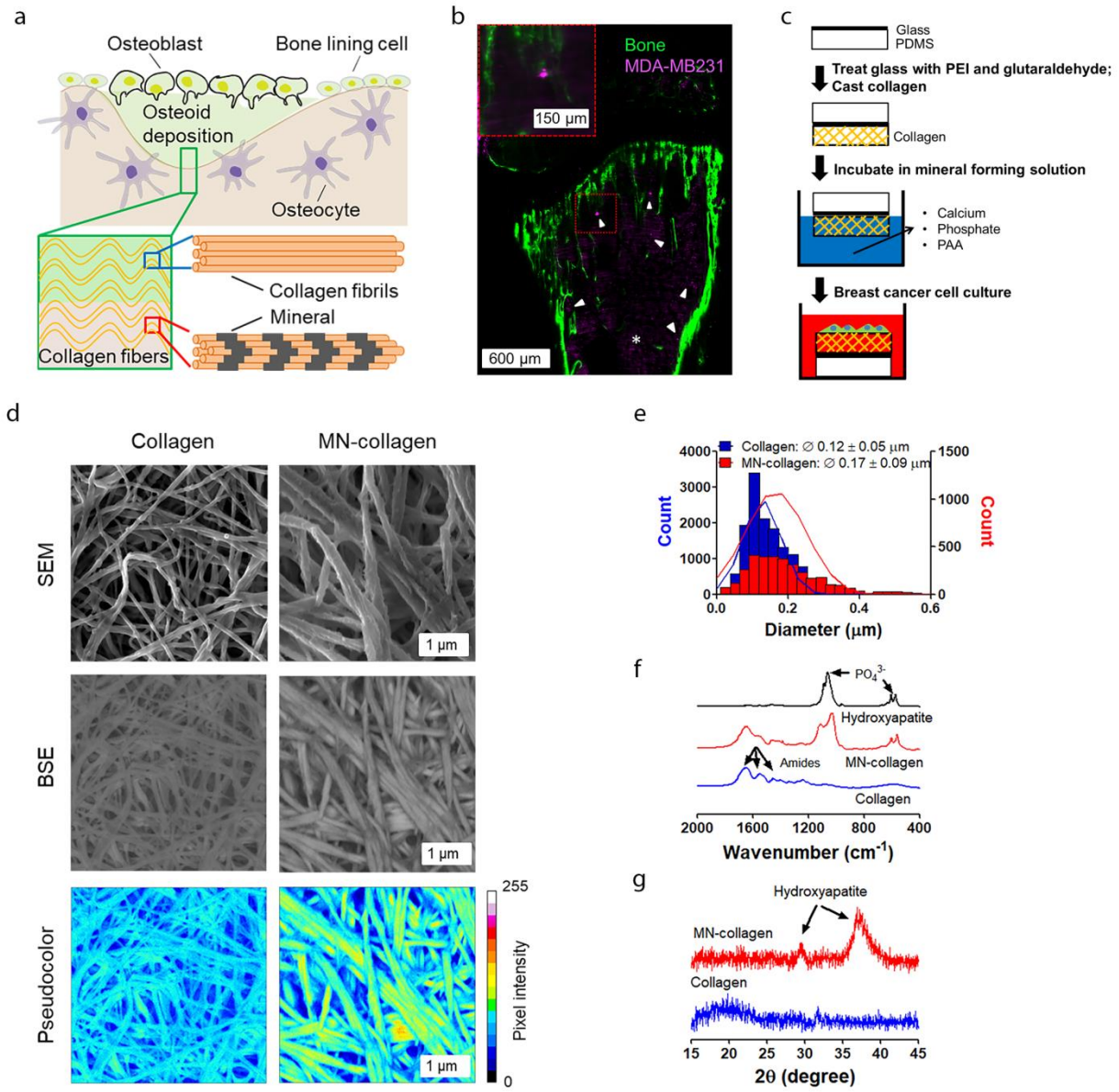

Figure 1: Engineered bone matrix models to study tumor cell interactions with mineralized collagen. a, Schematic of bone ECM formation in osteogenic niches. Osteoblasts first deposit osteoid, which consists primarily of collagen type I fibers (blue box) that become mineralized (red box) over time by intrafibrillar mineralization. **b,** Intracardially injected MDA-MB231 labeled with Cy5-containing silica nanoparticles (magenta) disseminate to regions in which new bone matrix becomes mineralized as visualized by light sheet imaging of a calcein-labeled, cleared mouse tibia (green). White arrow-heads and * indicate MDA-MB231 cells and autofluorescence of bone marrow, respectively. Scale bar = 600 µm and 150 µm (inset). **c**, Experimental setup to mineralize fibrillar collagen type I matrices via the PILP method for subsequent analysis of breast cancer cell phenotype. PDMS: Polydimethylsiloxane; PEI: polyethyleneimine; PAA: polyaspartic acid. **d**, Representative SEM and BSE images visualizing the fibrillar nature and mineral content

bioRxiv preprint doi: https://doi.org/10.1101/2022.06.29.498001; this version posted July 2, 2022. The copyright holder for this preprint (which was not certified by peer review) is the author/funder. All rights reserved. No reuse allowed without permission.

of collagen and mineralized collagen (MN-collagen) substrates. Pseudocolor indicates mineral content as determined from BSE images. Scale bar = 1 µm. **e**, Fibril diameter (Ø) of control and mineralized collagen substrates quantified from SEM images. **f**, FT-IR spectra of the different collagen substrates and highly crystalline hydroxyapatite particles as control. Arrows indicate phosphate (450 - 750 cm^{-1} and 900 - 1300 cm^{-1}) and amide peak areas (1200 - 1700 cm^{-1}). **g**, pXRD patterns indicate the presence of hydroxyapatite in mineralized, but not control collagen.

bioRxiv preprint doi: https://doi.org/10.1101/2022.06.29.498001; this version posted July 2, 2022. The copyright holder for this preprint (which was not certified by peer review) is the author/funder. All rights reserved. No reuse allowed without permission.

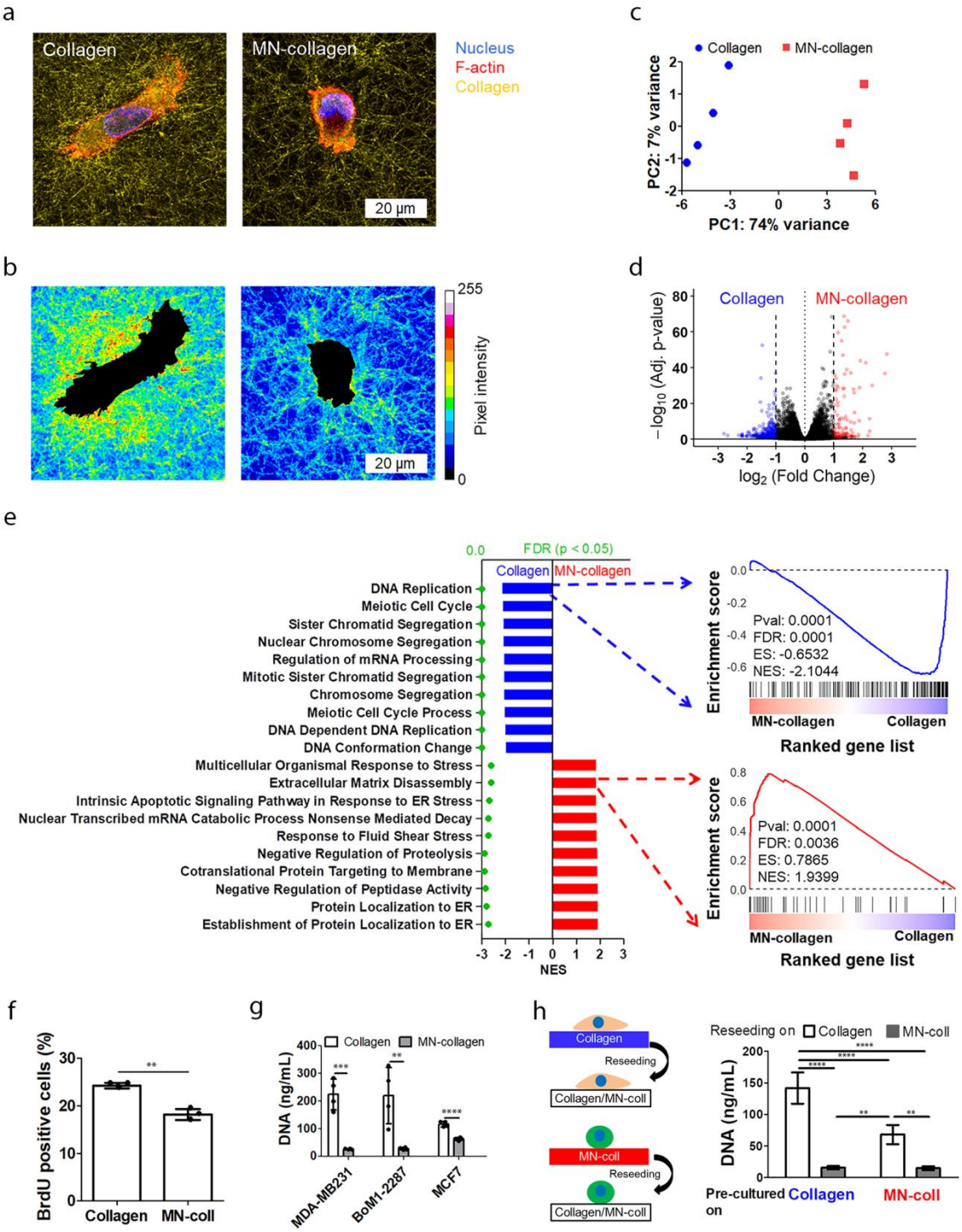

Figure 2: Mineralization of collagen alters breast cancer cell gene expression and growth. a, MDA-MB231 morphology and collagen network structure 5 h after seeding visualized via confocal reflectance microscopy. **b,** Pseudo-colored reflectance intensity maps indicate differences in collagen remodeling between both conditions. Scale bar = 20 µm. **c-e,** Effect of collagen mineralization on MDA-MB231 gene expression determined by principal component analysis (PCA) (c), differential gene expression analysis (n = 4) (d), and gene set enrichment

bioRxiv preprint doi: https://doi.org/10.1101/2022.06.29.498001; this version posted July 2, 2022. The copyright holder for this preprint (which was not certified by peer review) is the author/funder. All rights reserved. No reuse allowed without permission.

analysis (GSEA) (e) of bulk RNA-seq data collected after 7 d of culture on the different substrates. In d, genes colored in red are upregulated by cells cultured on mineralized collagen, while genes colored in blue are upregulated on collagen. For GSEA, the top 10 enriched pathways in cells cultured on collagen and mineralized collagen were derived from GO biological process. Green dots indicate false discovery rates (FDR). Normalized enrichment scores (ES) are denoted by NES. **f**, BrdU image analysis and **g,** fluorimetric quantification of DNA content of MDA-MB231 cultured for 7 d on the different substrates (n = 4). **h**, Analysis of MDA-MB231 growth following 7 days of pre-culture on the different substrates (n = 4). **: $P < 0.01$, ***: $P < 0.001$, ****: $P < 0.0001$.

bioRxiv preprint doi: https://doi.org/10.1101/2022.06.29.498001; this version posted July 2, 2022. The copyright holder for this preprint (which was not certified by peer review) is the author/funder. All rights reserved. No reuse allowed without permission.

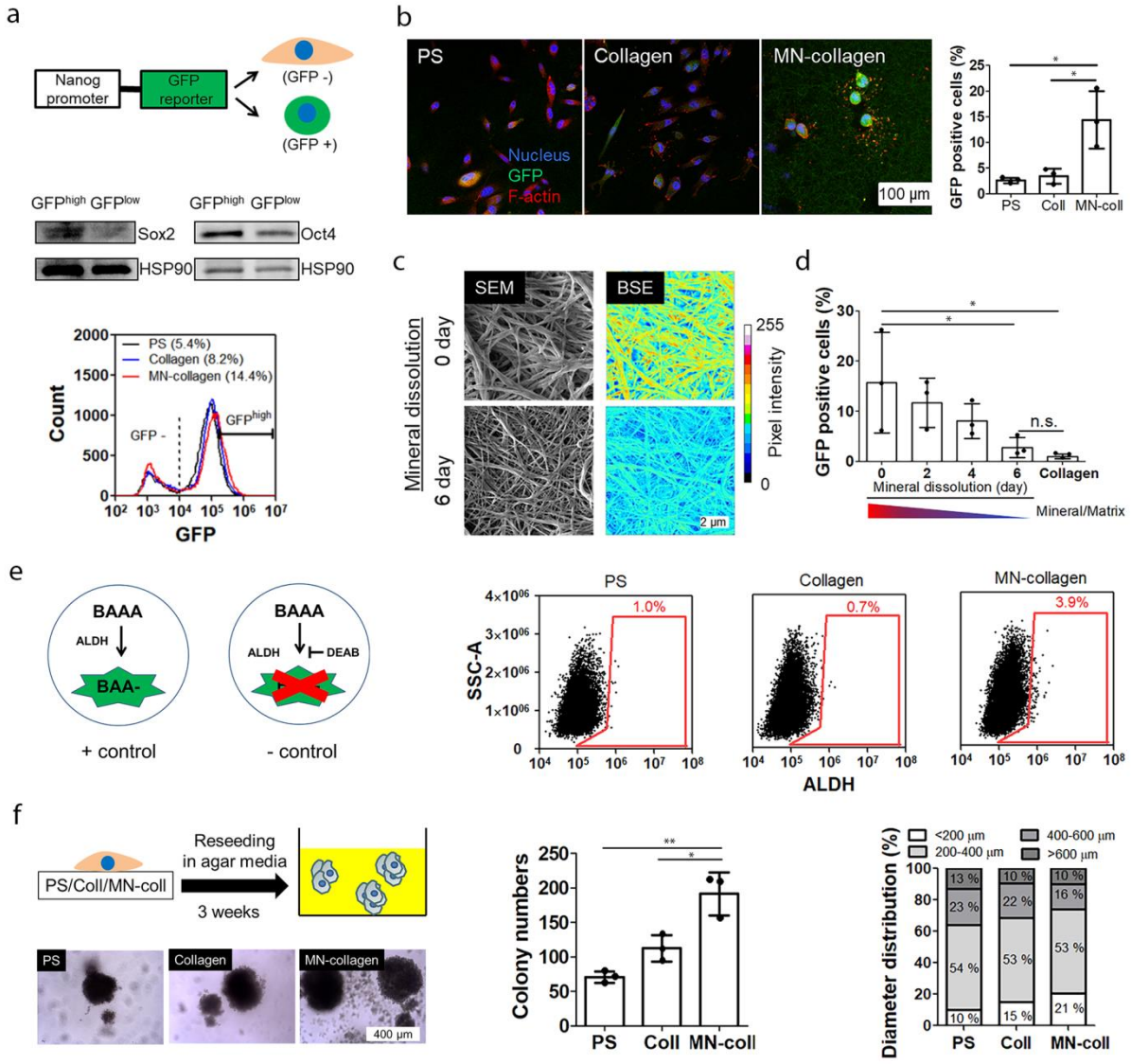

Figure 3: Collagen mineralization induces a stem-like phenotype in breast cancer cells. a, Schematic of the Nanog-MDA-MB231 reporter cell line in which increased GFP expression indicates a more stem-like phenotype (top). Western Blot analysis of Sox2 and Oct4 levels after FACS sorting of Nanog-MDA-MB231 reporter cells into GFP^{high} and GFP^{low} subpopulations (middle). Flow cytometry analysis of Nanog-MDA-MB231 reporter cells after 7 d of culture on polystyrene (PS), collagen, or mineralized collagen (bottom). **b,** Representative confocal micrographs and corresponding quantification of GFP positive cells after 7 d of culture on the different substrates (n = 3). Scale bar = 100 µm. **c**, **d**, Representative SEM and BSE (Pseudo-colored) images of mineralized collagen at different time point of dissolution and confocal image analysis of GFP positive cells as a function of collagen mineral content (n = 3). Mineral content of substrates was controlled by dissolution of hydroxyapatite over several days. One-way ANOVA post-hoc Dunnett's multiple comparison test. **e**, Analysis of aldehyde dehydrogenase (ALDH) activity in parental MDA-MB231 cells after 7 d of culture. Aminoacetaldehyde (BAAA) is

bioRxiv preprint doi: https://doi.org/10.1101/2022.06.29.498001; this version posted July 2, 2022. The copyright holder for this preprint (which was not certified by peer review) is the author/funder. All rights reserved. No reuse allowed without permission.

converted by ALDH into BODIPY-aminoacetate (BAA) that leads to increased intracellular fluorescence. Diethylaminobenzaldehyde (DEAB) inhibits ALDH and served as negative control. **f**, Soft agar colony formation after preculture of parental MDA-MB231 on the different substrates. Scale bar = 400 μm. Quantification of the number (n = 3) and size distribution of colonies larger than 100 μm in diameter *: $P < 0.05$, **: $P < 0.01$.

bioRxiv preprint doi: https://doi.org/10.1101/2022.06.29.498001; this version posted July 2, 2022. The copyright holder for this preprint (which was not certified by peer review) is the author/funder. All rights reserved. No reuse allowed without permission.

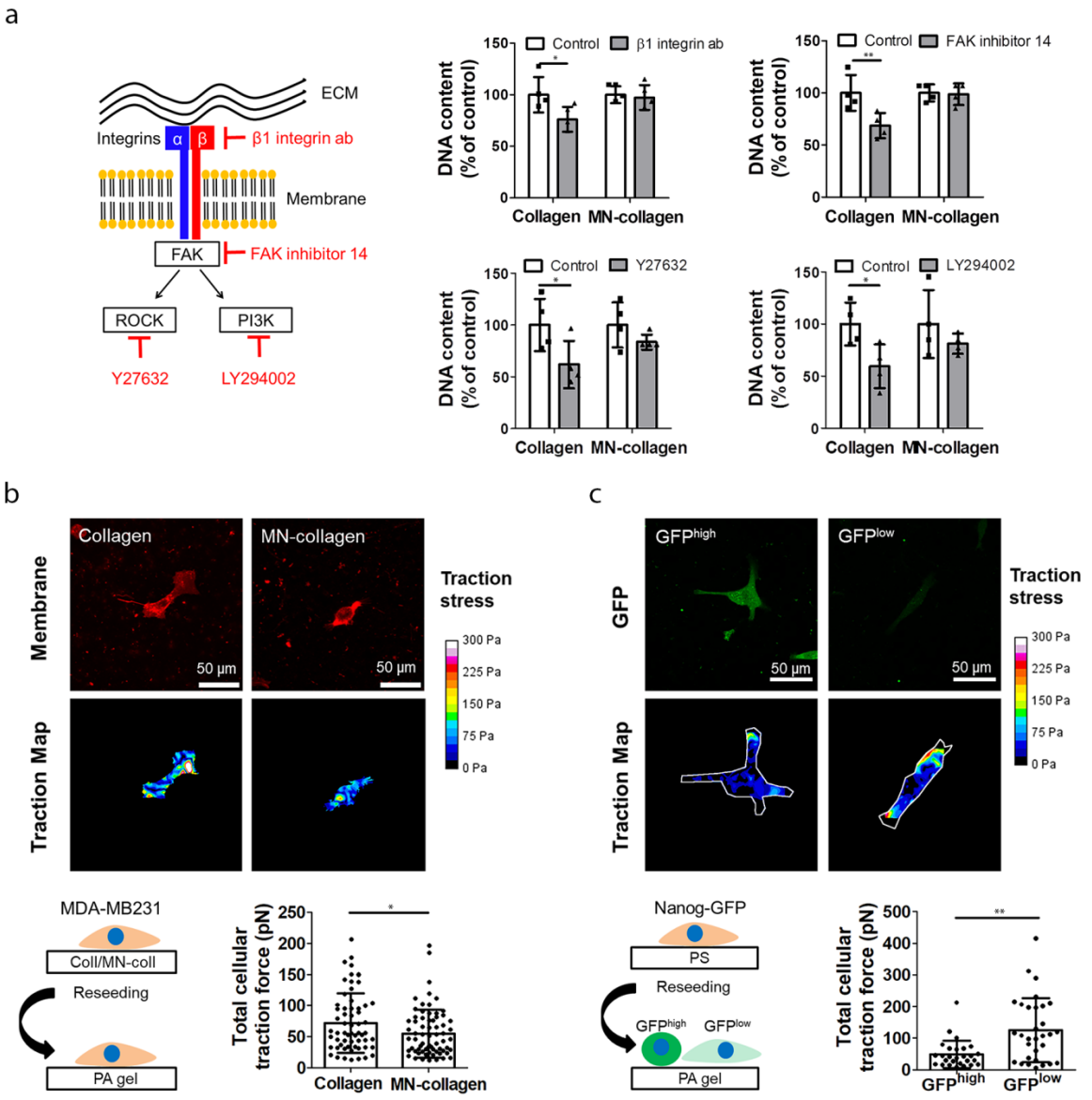

Figure 4: Collagen mineralization inhibits breast cancer cell mechanotransduction. a, Schematic of integrin-mediated mechanosignaling and effect of different mechanosignaling inhibitors on the growth of MDA-MB231 cells cultured on collagen and mineralized collagen (n = 4). **b,** Traction force microscopy of MDA-MB231 cells following preculture on collagen and mineralized collagen. Representative images of MemGlow 590-labeled cells (top), traction maps (middle), and corresponding quantification of traction forces (bottom). Scale bar = 50 µm. $P < 0.05$ by Mann-Whitney U-test. **c,** Traction force microscopy of GFP^{high} and GFP^{low} MDA-MB231 cells. Representative fluorescence images (top), traction maps (middle), and corresponding quantification of traction forces (bottom) of Nanog-GFP cells. White lines on traction maps indicate contour of cell. Scale bar = 50 µm. $P < 0.05$ by Mann-Whitney U-test. *: $P < 0.05$, **: $P < 0.01$.

bioRxiv preprint doi: https://doi.org/10.1101/2022.06.29.498001; this version posted July 2, 2022. The copyright holder for this preprint (which was not certified by peer review) is the author/funder. All rights reserved. No reuse allowed without permission.

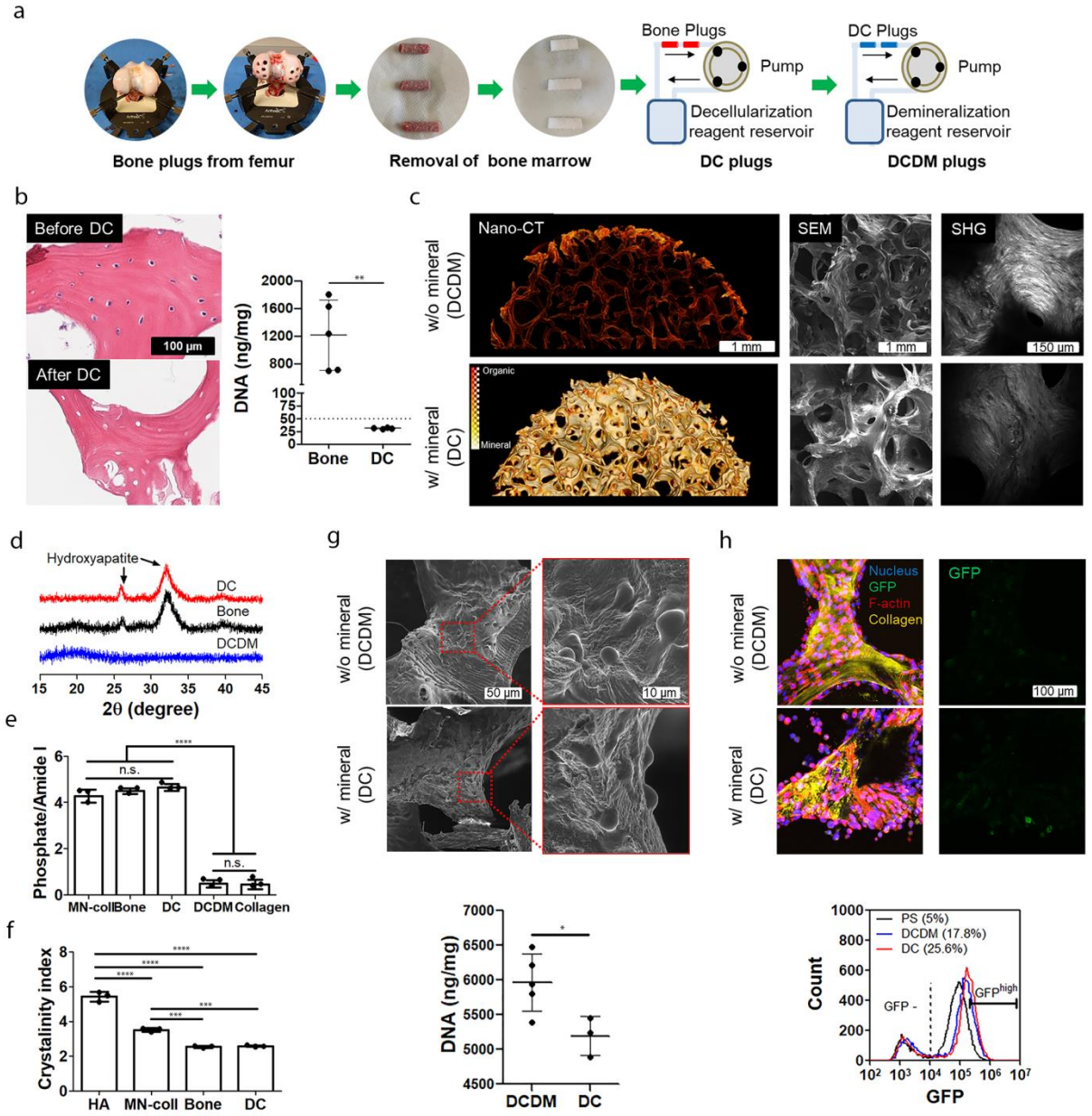

Figure 5: Physiological bone scaffolds to test the effect of bone mineral on the stem-like phenotype of MDA-MB231. a, Schematic visualizing the preparation of decellularized (DC) and decellularized/demineralized (DCDM) bone scaffolds from 1-2 cm long, 6mm diameter neonatal bovine femur bone plugs. **b**, H&E staining and DNA quantification of scaffolds after DC process (Bone: n = 5, DC: n = 3). Scale bar = 100 µm. **c**, Nano-CT, SEM and second harmonic generation (SHG) images of scaffolds after DCDM process. Scale bar = 1 mm (Nano-CT and SEM) and 150 µm (SHG). **d-f**, pXRD analysis of mineral phase **(d)** and FT-IR analysis of mineral to matrix ratio (n = 3) **(e)** and cyrstallinity index (n = 3**) (f)** after DC and DCDM process. Commercially available hydroxyapatite (HA) served as control. **g**, SEM images and DNA quantification of MDA-MB231 cells cultured on the different scaffolds (DCDM: n = 5, DC: n = 3). Scale bar = 50 µm (left) and

bioRxiv preprint doi: https://doi.org/10.1101/2022.06.29.498001; this version posted July 2, 2022. The copyright holder for this preprint (which was not certified by peer review) is the author/funder. All rights reserved. No reuse allowed without permission.

10 μm (right). **h**, Confocal images and flow cytometry analysis of Nanog-GFP cells cultured on the different scaffolds. Scale bar = 100 μm. *: $P < 0.05$, **: $P < 0.01$, ***: $P < 0.001$, ****: $P < 0.0001$.

bioRxiv preprint doi: https://doi.org/10.1101/2022.06.29.498001; this version posted July 2, 2022. The copyright holder for this preprint (which was not certified by peer review) is the author/funder. All rights reserved. No reuse allowed without permission.

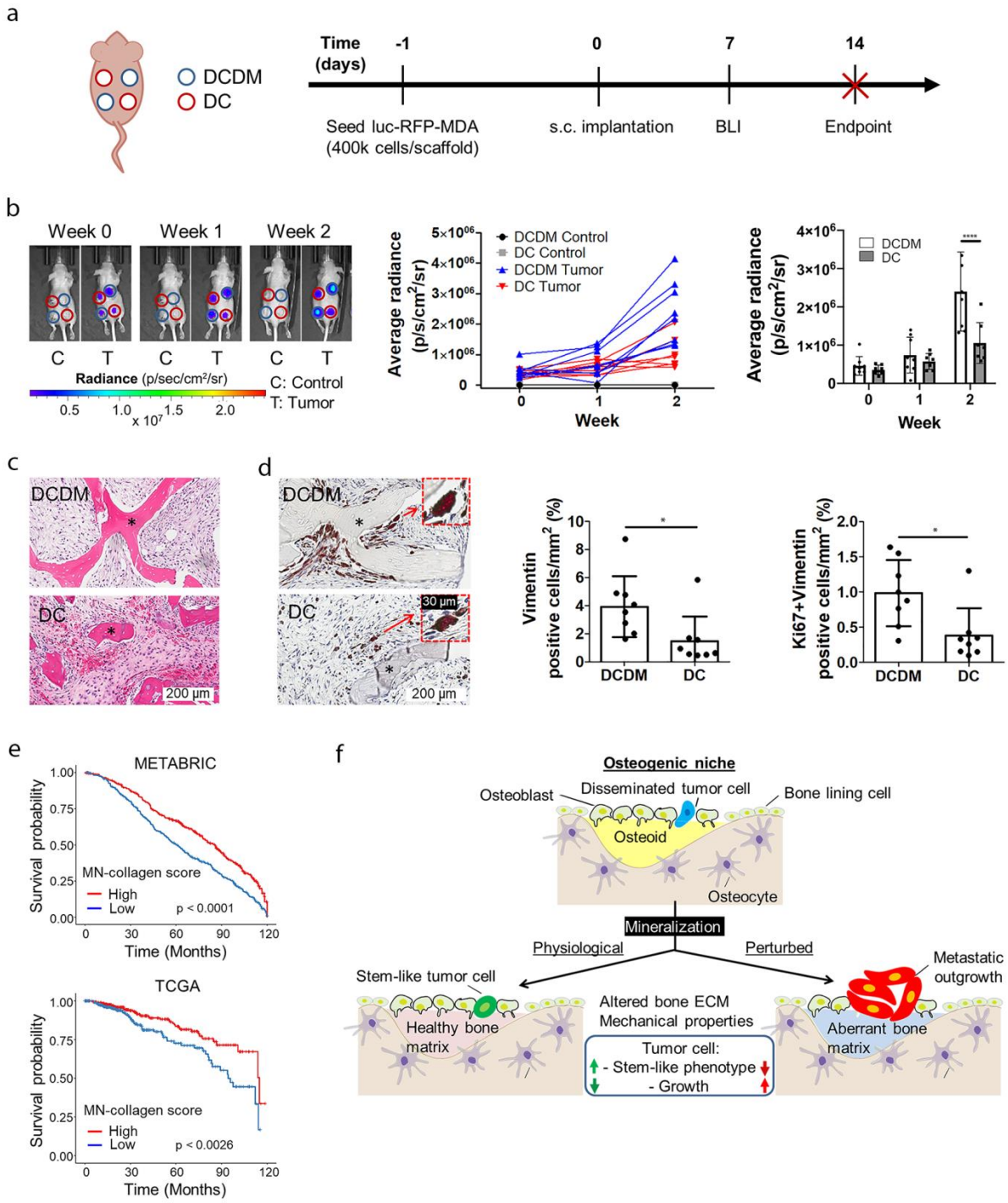

Figure 6: Mineralized bone matrix reduces tumor growth *in vivo,* and mineral-induced gene expression signature correlates with improved patient prognosis. a, Time course of xenograft experiment involving implantation of MDA-MB231-seeded DCDM and DC scaffolds into female nude mice. **b**, Representative bioluminescence intensity (BLI) images and BLI quantification of tumor growth on the different bone scaffolds (DCDM: $n = 8$, DC: $n = 7$). **c,d,** Representative H&E images (c) and IHC images and analysis of vimentin and vimentin/Ki67 positive cells ($n = 8$**)** (d)

bioRxiv preprint doi: https://doi.org/10.1101/2022.06.29.498001; this version posted July 2, 2022. The copyright holder for this preprint (which was not certified by peer review) is the author/funder. All rights reserved. No reuse allowed without permission.

in implanted bone scaffolds. Scale bar = 200 µm and 30 µm (inset). * = scaffold. **e,** Overall survival of breast cancer patients scoring high or low for expression of mineral-induced gene signatures (Table 2) using the METABRIC and TCGA cohorts. **f,** Proposed relationship between bone ECM and breast cancer cell phenotype. Our results suggest that mineralization of collagen type I-rich osteoid in osteogenic niches induces stem-like, less-proliferative phenotypes in breast cancer cells. As bone matrix mineralization changes (e.g. due to aging etc.), tumor cell growth is activated possibly due to bone matrix-dependent changes in tumor cell mechanosignaling. *: $P < 0.05$, ****: $P < 0.0001$.